JCB Journal of Cell Biology

ARTICLE

BAR scaffolds drive membrane fission by crowding disordered domains

Wilton T. Snead[1], Wade F. Zeno[1], Grace Kago[1,3], Ryan W. Perkins[1], J Blair Richter[2], Chi Zhao[1], Eileen M. Lafer[2], and Jeanne C. Stachowiak[1,3]

Cellular membranes are continuously remodeled. The crescent-shaped bin-amphiphysin-rvs (BAR) domains remodel membranes in multiple cellular pathways. Based on studies of isolated BAR domains in vitro, the current paradigm is that BAR domain–containing proteins polymerize into cylindrical scaffolds that stabilize lipid tubules. But in nature, proteins that contain BAR domains often also contain large intrinsically disordered regions. Using in vitro and live cell assays, here we show that full-length BAR domain–containing proteins, rather than stabilizing membrane tubules, are instead surprisingly potent drivers of membrane fission. Specifically, when BAR scaffolds assemble at membrane surfaces, their bulky disordered domains become crowded, generating steric pressure that destabilizes lipid tubules. More broadly, we observe this behavior with BAR domains that have a range of curvatures. These data suggest that the ability to concentrate disordered domains is a key driver of membrane remodeling and fission by BAR domain–containing proteins.

Introduction

Cellular membranes must undergo dynamic remodeling to facilitate essential cellular processes, including formation of trafficking vesicles (Conner and Schmid, 2003), viral egress (Hurley et al., 2010), and cytokinesis (Mierzwa and Gerlich, 2014). Since membranes resist deformation (Helfrich, 1973), cells employ specialized protein machines to drive membrane remodeling (Zimmerberg and Kozlov, 2006). For example, the crescent-shaped, dimeric bin-amphiphysin-rvs (BAR) domains (Frost et al., 2009; Mim and Unger, 2012; Simunovic et al., 2015) polymerize into cylindrical scaffolds on membrane surfaces, forcing the underlying membrane to adopt the tubular geometry of the scaffold (Frost et al., 2008; Mim et al., 2012; Adam et al., 2015). This rigid scaffold has been hypothesized to stabilize membrane tubules, preventing their division into separate membrane compartments through the process of membrane fission (Boucrot et al., 2012). Notably, this perspective comes primarily from studies performed in vitro. In living cells, BAR scaffolds are thought to assemble into more limited scaffolds that shape membranes in concert with other proteins, including the dynamin fission machine and the actin cytoskeleton (Itoh et al., 2005; Ferguson et al., 2009; Renard et al., 2015).

Importantly, many in vitro studies on the membrane shaping behavior of BAR domains have examined the BAR domain in isolation, with significant portions of the protein removed. Examples include the N-terminal amphipathic helix BAR (N-BAR) domain of amphiphysin (Peter et al., 2004), the FCH BAR (F-BAR) domain of FCHo1/2 (Henne et al., 2007, 2010), the F-BAR domain of the neuronal migration protein srGAP2 (Guerrier et al., 2009), the F-BAR domains of the cytokinesis proteins Imp2 (McDonald et al., 2016) and Cdc15 (McDonald et al., 2015), and the inverted BAR (I-BAR) domains of MIM and ABBA (Mattila et al., 2007; Saarikangas et al., 2009), among others. These results have provided critical insight into the detailed geometry of BAR domain arrangement at membrane surfaces, helping to elucidate their mechanisms of membrane curvature sensing and induction. However, BAR domains do not typically exist in isolation in the cell, but rather as part of large, multi-domain proteins that also frequently contain long, intrinsically disordered protein (IDP) domains of several hundred amino acids (Miele et al., 2004; Lee et al., 2007; Henne et al., 2010; Roberts-Galbraith and Gould, 2010; Wuertenberger and Groemping, 2015). How might these disordered domains influence the membrane remodeling behavior of BAR domains?

Recent work from our laboratory (Stachowiak et al., 2010, 2012) and others (Vennema et al., 1996; Bhagatji et al., 2009; Copic et al., 2012; Jiang et al., 2013; Wu et al., 2014) has revealed that molecular crowding among proteins attached to membrane surfaces at high density generates steric pressure, which provides a potent force for membrane shaping. Further, previous work found that disordered domains, which occupy large footprints on the membrane surface in comparison to well-folded

[1]Department of Biomedical Engineering, University of Texas at Austin, Austin, TX; [2]Department of Biochemistry and Structural Biology, Center for Biomedical Neuroscience, University of Texas Health Science Center at San Antonio, San Antonio, TX; [3]Institute for Cellular and Molecular Biology, University of Texas at Austin, Austin, TX.

Correspondence to Jeanne C. Stachowiak: jcstach@austin.utexas.edu.

https://doi.org/10.1083/jcb.201807119

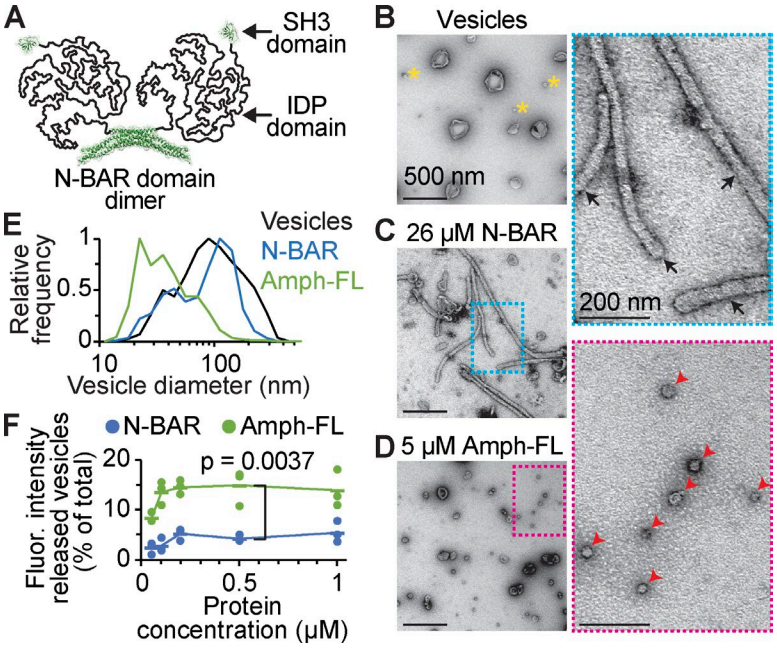

Figure 1. **Amphiphysin drives membrane fission, while the N-BAR domain stabilizes membrane tubules.** Membrane composition for vesicles in TEM: 80 mol% DOPC, 5 mol% PtdIns(4,5)P_2, and 15 mol% DOPS. SUPER template membrane composition: 79 mol% DOPC, 5 mol% PtdIns(4,5)P_2, 15 mol% DOPS, and 1 mol% Texas Red–DHPE. **(A)** Schematic of Amph-FL dimer. BAR domain: PDB 4ATM. SH3 domain: PDB 1BB9. **(B–D)** Negative stain TEM micrographs of 200 nm extruded vesicles before exposure to protein (B), after exposure to 26 µM N-BAR (C), and after exposure to 5 µM Amph-FL (D). Dashed boxes indicate zoomed regions to the right. Black arrows indicate membrane tubules; red arrowheads indicate fission vesicles. Yellow asterisks indicate small vesicles that are present in the vesicle population before protein exposure. **(E)** Histograms of vesicle diameters measured from electron micrographs. Vesicles alone: n = 1,302 vesicles. 26 µM N-BAR: n = 462 vesicles. 5 µM Amph-FL: n = 1,071 vesicles. **(F)** Membrane release from SUPER templates, measured as Texas Red signal present in the supernatant after sedimentation of the SUPER templates. Membrane release in the absence of protein was measured and subtracted as background. Dots indicate data and lines indicate mean; n = 3 independent experiments. P value: one-tailed, unpaired Student's t test. (B–D) Bars, 500 nm; insets, 200 nm. See also Fig. S1 and Videos 1, 2, 3, 4, and 5.

proteins of equal molecular weight (Hofmann et al., 2012), enhanced the efficiency of membrane bending and fission (Busch et al., 2015; Snead et al., 2017). However, a fundamental, unanswered question has limited the potential of protein crowding to explain membrane remodeling in cells—what brings bulky domains together to generate steric pressure? In particular, what keeps crowded proteins from simply diffusing away from one another, dissipating steric pressure and inhibiting membrane shaping? Proteins such as amphiphysin (Miele et al., 2004; Peter et al., 2004) and FCHo1/2 (Henne et al., 2007, 2010), which contain both scaffold-forming BAR domains and bulky disordered domains, present a possible solution to this problem. Specifically, the ability of BAR domains to form scaffolds has the potential to locally concentrate disordered domains such that steric pressure is amplified rather than dissipated.

Therefore, we set out to investigate the impact of disordered domains on the membrane remodeling ability of BAR proteins. To our surprise, we found that while isolated BAR domains formed stable membrane tubules, full-length amphiphysin (Amph-FL) and FCHo1 destabilized these tubules, leading to highly efficient membrane vesiculation. These results suggest that BAR domain–containing proteins can act as templates that locally amplify steric pressure among disordered domains, leading to membrane fission.

Results

While the amphiphysin N-BAR domain stabilizes membrane tubules, Amph-FL drives membrane vesiculation

Amphiphysin, an important component of the vesicle recycling machinery (Di Paolo et al., 2002), is composed of an N-BAR domain, followed by an IDP domain of ∼383 amino acids in humans, and a C-terminal SH3 domain (Owen et al., 1998, 2004; Miele et al., 2004; Peter et al., 2004; Fig. 1 A). To compare the membrane remodeling abilities of Amph-FL to those of the N-BAR domain alone, we first examined the effects of each protein on giant unilamellar vesicles (GUVs). These experiments revealed that both the N-BAR domain and Amph-FL drove potent membrane bending within 10 min of mixing vesicles and protein, forming mobile, diffraction-limited tubules that extended from the GUV surface (Fig. S1 A and Videos 1 and 2). These GUVs often collapsed or broke apart into smaller tubules and fragments later during imaging (Fig. S1 A and Videos 3, 4, and 5), suggesting that lipid tubule formation was not the endpoint of the membrane remodeling process.

To directly visualize membrane morphology at the end of remodeling (after 30 min incubation at 37°C), we used negative stain transmission EM (TEM) to resolve membrane structures below the optical diffraction limit. As expected from previous findings (Peter et al., 2004; Gallop et al., 2006), the N-BAR domain transformed vesicles that had an average initial diameter of 200 nm into long tubules with average outer diameter 44 ± 6 nm SD (Fig. 1, B and C; and Fig. S1, B and C). In contrast, Amph-FL did not drive appreciable membrane tubule formation in TEM experiments. Rather, Amph-FL divided the vesicles of initially 200-nm diameter into a population of highly curved vesicles with a peak diameter centered near 22 nm (Fig. 1, D and E; and Fig. S1 D). This finding suggests that formation of membrane tubules is not a stable endpoint of membrane remodeling driven by Amph-FL, as observed in GUV experiments (Fig. S1 A). In contrast, N-BAR did not drive a substantial shift in the vesicle diameter distribution in TEM experiments (Fig. 1 E). Collectively, these results suggest that Amph-FL is capable of driving membrane fission, a more energetically demanding process than membrane tubule formation (Campelo and Malhotra, 2012).

Amph-FL generates highly curved fission products

To better understand the ability of amphiphysin to drive membrane fission, we compared N-BAR and Amph-FL in two additional assays of membrane fission. In the first of these experiments, we used supported bilayers with extra

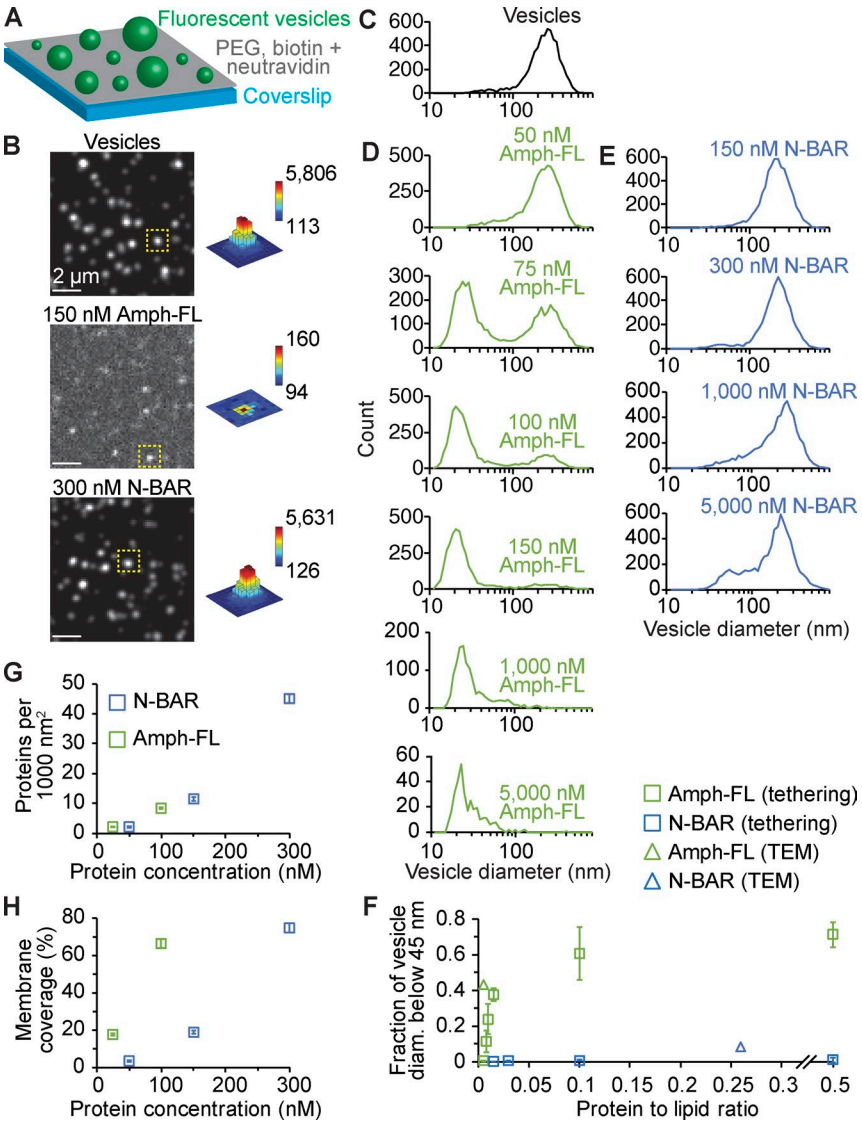

Figure 2. **Amph-FL produces highly curved fission products.** Tethered vesicle composition: 76 mol% DOPC, 5 mol% PtdIns(4,5)P_2, 15 mol% DOPS, 2 mol% Oregon Green 488–DHPE, and 2 mol% DP-EG10-biotin. **(A)** Schematic of tethered vesicle fission experiment. **(B)** Representative spinning disc confocal micrographs of tethered vesicles before exposure to protein (top), after exposure to 150 nM Amph-FL (middle), and after exposure to 300 nM N-BAR (bottom). Contrast settings in top and bottom images are the same while contrast in middle image is adjusted to clearly show vesicle puncta. Dashed yellow boxes indicate puncta intensity profiles on the right, where bar heights are all scaled between 90 and 6,000 brightness units while each color map corresponds to the specified intensity range. **(C–E)** Distributions of vesicle diameter measured by tethered vesicle assay before exposure to protein (C), after exposure to Amph-FL at the specified concentrations (D), and after exposure to N-BAR at the specified concentrations (E). **(F)** Summary of tethered vesicle and TEM experiments, expressed as the proportion of vesicle diameters within the high curvature group of 45 nm or smaller. Markers for tethered vesicle data represent mean ± first SD; $n = 3$ independent experiments. TEM data from Fig. 1 E. **(G)** Number of membrane-bound proteins per 1,000 nm² of membrane surface area versus concentration of N-BAR or Amph-FL. **(H)** Data in G plotted as the coverage of the membrane surface by proteins as a function of protein concentration. Error bars in G and H represent 95% CI; $n > 1{,}700$ vesicles for each condition. Amph-FL and N-BAR data collected using 30-nm–extruded vesicles and sonicated vesicles, respectively (see Materials and methods). (B) Bars, 2 µm. See also Figs. S1, S2, and S3.

membrane reservoir (SUPER) templates, which are glass beads surrounded by a low-tension membrane. Exposure of SUPER templates to fission-driving proteins results in measurable membrane release from the beads (Pucadyil and Schmid, 2008; Liu et al., 2011; Neumann et al., 2013). SUPER template experiments revealed that while both N-BAR and Amph-FL drove membrane release in the concentration range of 50 to 1,000 nM, Amph-FL drove more than twice as much (2.6 to 4.7-fold greater) membrane release at each concentration (Fig. 1 F). Amph-FL also drove consistently greater levels of membrane release compared with the epsin N-terminal homology (ENTH) domain, a protein previously shown to drive membrane fission (Snead et al., 2017; Fig. S1 E). Notably, the apparent plateau in membrane release (Fig. 1 F) may be due to the fact that some of the SUPER template membrane interacts closely with the bead surface, increasing the barrier to membrane release, as seen in previous reports (Liu et al., 2011; Neumann and Schmid, 2013; Snead et al., 2017). However, substantially higher concentrations of Amph-FL up to 10 µM drove further membrane release (Fig. S1 E).

Notably, membrane release does not directly imply efficient membrane vesiculation, as both vesicles and lipid tubules can be shed from SUPER templates. Therefore, we next employed a tethered vesicle assay to quantify the distributions of vesicle diameter over a range of protein concentrations (Snead et al., 2017). Specifically, we tethered fluorescent vesicles to a coverslip passivated with polyethylene glycol (PEG) and PEG-biotin (Fig. 2 A). Vesicles in these experiments contained a biotinylated lipid, which facilitated tethering to the substrate through binding to neutravidin. Vesicles also contained the fluorescent lipid Oregon Green 488–1,2-dihexadecanoyl-*sn*-glycero-3-phosphoethanolamine (DHPE), which we used to quantify the brightness of each vesicle after imaging in confocal fluorescence microscopy (Aguet et al., 2013; Fig. 2 B). We then converted the resulting distributions of vesicle brightness to approximate distributions of vesicle diameter by calibrating against the initial vesicle diameter distribution measured using dynamic light scattering (see Materials and methods).

Using this assay, we found that Amph-FL in the concentration range of 50–150 nM transformed vesicles with an average initial

diameter of 200 nm (Fig. 2, B and C) to a population of high curvature fission products (Fig. 2, B and D) with a median diameter of 22 nm at 150 nM, in agreement with results from TEM (Fig. 1, D and E). The proportion of vesicles that fell within the high curvature group (diameters below ∼45 nm) increased with increasing protein concentration, from less than 1% at 50 nM to ∼38% at 150 nM (Fig. 2 F). Importantly, the biotinylated lipid alone did not drive fission in the absence of protein (Fig. 2 C). Interestingly, fission by Amph-FL was highly cooperative, leading to a bimodal distribution of vesicle diameter (Fig. 2 D). In contrast, previous studies using the same assay found that membrane fission by the ENTH domain resulted in a gradual shift of the size distribution toward smaller diameters (Snead et al., 2017). We speculate that local self-assembly of Amph-FL into membrane-bound scaffolds may drive budding of small vesicles directly from larger vesicles, resulting in a bimodal distribution of vesicle diameter.

The isolated N-BAR domain did not drive fission even at higher protein concentrations in comparison to Amph-FL (Fig. 2, B, E, and F). Some long, nondiffraction-limited lipid tubules were visible on occasion in tethered vesicle experiments with N-BAR (Fig. 2 B), but our estimations of vesicle diameter did not change substantially if such puncta were excluded (Fig. S1 F). Tubules became more prevalent at micromolar N-BAR concentrations (Fig. S1 G), consistent with the tubules formed in TEM experiments (Fig. 1 C). However, N-BAR did not drive substantial vesiculation at micromolar concentrations, consistent with our findings from TEM (Fig. 2, E and F). Our results are in agreement with previous studies that have reported membrane tubulation by N-BAR at protein to lipid ratios of ∼1:100 (Peter et al., 2004; Ambroso et al., 2014; Isas et al., 2015), the range in which we observed potent membrane fission by Amph-FL (Fig. 2 F). However, previous work has reported membrane vesiculation by the isolated N-BAR domain of amphiphysin at substantially higher protein-to-lipid ratios (Peter et al., 2004), in contrast with our findings at similarly high ratios (Fig. 2 F). Additionally, the isolated N-BAR domain of endophilin at a protein to lipid ratio of ∼1:100 has been reported to drive membrane vesiculation (Poudel et al., 2016). The differences between these reports and our findings may be due to differences in lipid composition, differences between the amphiphysin and endophilin N-BAR domains, or differences in other experimental parameters. Notably, higher concentrations of Amph-FL were required to observe fission in TEM experiments compared with tethered vesicle experiments. This increase is due to the high lipid concentration used in TEM experiments (∼100-fold greater than tethered vesicle experiments), which is necessary to obtain an adequate density of lipid structures for TEM (Fig. 2 F; see Materials and methods). Taken together, our results from EM and tethered vesicle experiments confirm that Amph-FL is a potent driver of membrane fission, while the isolated N-BAR domain primarily forms membrane tubules.

The ability of Amph-FL to drive membrane fission does not arise from greater membrane binding affinity in comparison to isolated N-BAR

How can we explain the ability of Amph-FL to drive membrane fission? One possible explanation could be that the full-length protein may bind more strongly to membrane surfaces compared with the N-BAR domain alone, resulting in more potent membrane remodeling. To examine this possibility, we used a tethered vesicle assay similar to the experiments described above to quantify the relative extent of protein–membrane binding. In this assay, proteins were labeled with Atto 594 dye, while vesicles contained the lipid Oregon Green 488–DHPE. We quantified vesicle diameter as described above, and used measurements of single fluorophore brightness to quantify the number of bound proteins per vesicle (Snead et al., 2017; see Materials and methods). From these measurements we determined the density of membrane-bound proteins, which increased with increasing protein concentration in solution (Fig. S2, A–C). These experiments revealed that over the range of protein concentrations in which membrane remodeling and vesiculation began to occur, Amph-FL and N-BAR reached similar number densities of membrane-bound protein, indicating that the two proteins bind membranes with similar affinity (Fig. 2 G). Specifically, these results suggest that the disordered domain did not significantly enhance protein–lipid and protein–protein interactions, either of which would be expected to increase the density of membrane-bound protein. Indeed, the isolated disordered domain of amphiphysin showed no detectable binding to the membranes used in fission studies with Amph-FL (Fig. S2 D). Therefore, the ability of Amph-FL to drive membrane fission cannot be explained by differences in membrane recruitment. However, Amph-FL reached a high coverage of the membrane surface at substantially lower protein concentration compared with N-BAR, owing to the larger membrane footprint of Amph-FL (Fig. 2 H; see Materials and methods). These findings help explain how Amph-FL reached a crowded coverage of the membrane surface, sufficient to drive membrane vesiculation.

The disordered domain of amphiphysin drives membrane fission on its own, but requires higher protein concentration compared with Amph-FL

Another possible explanation for the ability of amphiphysin to drive membrane fission is that its substantial disordered domain (residues 240–622) generates steric pressure that promotes fission, in line with previous studies on other membrane-bound disordered domains (Busch et al., 2015; Snead et al., 2017). If so, the isolated disordered domain should be able to drive membrane fission when bound to membrane surfaces at sufficient density. To test this idea, we purified the disordered domain of amphiphysin, lacking the C-terminal SH3 domain (Amph CTD ΔSH3; Fig. 3 A). We first performed fluorescence correlation spectroscopy (FCS) measurements to quantify the hydrodynamic radius of this domain. Specifically, we calibrated the diffusion time of Amph CTD ΔSH3 against the diffusion times of two protein standards with known hydrodynamic radii, transferrin (Hall et al., 2002) and the C-terminal domain of AP180 (AP180 CTD; Busch et al., 2015). These experiments yielded an approximate hydrodynamic radius for Amph CTD ΔSH3 of 4 nm (Fig. S2, E–G; see Materials and methods), which corresponds to a radius of gyration of ∼5 nm (Sherman and Haran, 2006; Hofmann et al., 2012), comparable to other disordered domains of similar molecular weight (Kalthoff et al., 2002; Busch et al., 2015). FCS

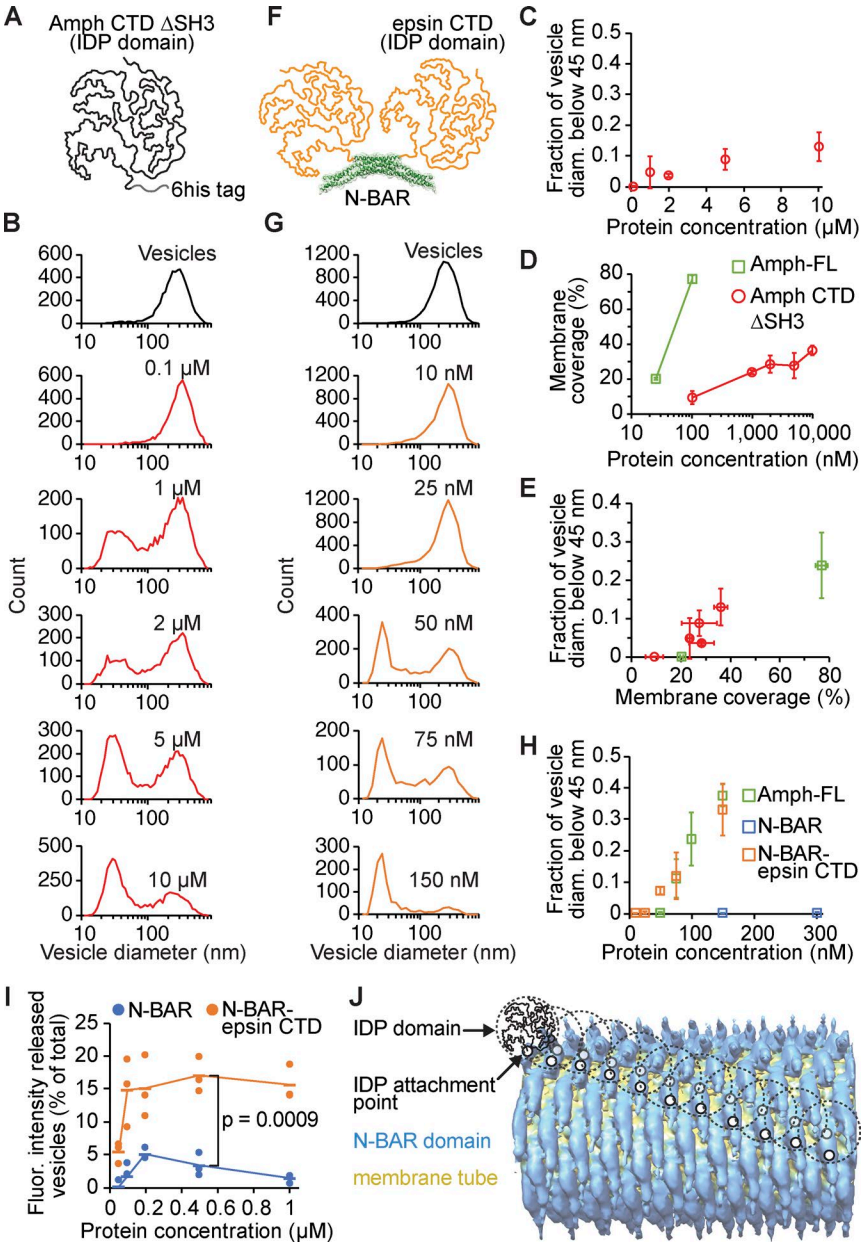

Figure 3. **The disordered domain of amphiphysin alone drives membrane fission, but the N-BAR scaffold substantially enhances fission efficiency.** Membrane composition in Amph CTD ΔSH3 tethered vesicle experiments: 76 mol% DOPC, 20 mol% DOGS-NTA-Ni, 2 mol% Oregon Green 488–DHPE, and 2 mol% DP-EG10-biotin. In tethered vesicle experiments with N-BAR-epsin CTD, DOGS-NTA-Ni was replaced with 5 mol% PtdIns(4,5)P_2 and 15 mol% DOPS. SUPER template membrane composition: 79 mol% DOPC, 5 mol% PtdIns(4,5)P_2, 15 mol% DOPS, and 1 mol% Texas Red–DHPE. **(A)** Schematic of Amph CTD ΔSH3. **(B)** Tethered vesicle fission experiments show that Amph CTD ΔSH3 forms highly curved fission products. **(C)** Summary of data from tethered vesicle fission experiments with Amph CTD ΔSH3 expressed as the ratio of the distribution area below 45 nm to the total distribution area (compare to Fig. 2 F). **(D)** Coverage of the membrane surface by Amph CTD ΔSH3 and Amph-FL as a function of protein concentration. Amph-FL data from Fig. 2 H. **(E)** Fraction of vesicle diameters below 45 nm generated by Amph CTD ΔSH3 and Amph-FL versus coverage of the membrane surface by proteins. Amph-FL fission data from Figs. 2 F and S2 M. Amph CTD ΔSH3 fission data from Fig. 3 C. **(F)** Schematic of N-BAR-epsin CTD chimera dimer. **(G)** Tethered vesicle fission measurements show that N-BAR-epsin CTD generates highly curved fission vesicle populations over the concentration range of 10–150 nM, similar to Amph-FL (compare to Fig. 2 D). **(H)** Summary of data from tethered vesicle fission experiments with N-BAR-epsin CTD, expressed as the ratio of the distribution area below 45 nm to the total distribution area. Amph-FL and N-BAR data from Fig. 2 F. **(I)** SUP ER template membrane shedding experiments show that N-BAR-epsin CTD drives greater membrane release compared with N-BAR (compare to Fig. 1 F). Dots indicate data and lines indicate mean; $n = 3$ independent experiments. P value: one-tailed, unpaired Student's t test. Amph CTD ΔSH3 markers in C and D and all markers in H represent mean ± first SD; $n = 3$ independent experiments. **(J)** Schematic of the N-BAR scaffold (EMDB 3192; Adam et al., 2015) with attachment points of some of the disordered domains marked (two per N-BAR dimer). Dashed circles indicate approximate volumes occupied by undeformed disordered domains. See also Figs. S2 and S3.

experiments also showed that the size of Amph CTD ΔSH3 varied with the concentration of monovalent salt in the buffer (Fig. S2 H), consistent with the known sensitivity of highly charged disordered proteins to changes in ionic strength (Srinivasan et al., 2014). We next performed tethered vesicle experiments to assess membrane fission by Amph CTD ΔSH3. The protein included an N-terminal hexa-histidine (6his) tag to facilitate binding to membranes by the lipid 1,2-dioleoyl-sn-glycero-3-([N-[5-amino-1-carboxypentyl]iminodiacetic acid]succinyl), nickel salt (DOGS-NTA-Ni; Fig. 3 A). Experiments revealed that Amph CTD ΔSH3 drove the formation of highly curved fission products (Fig. 3, B and C). However, 100-fold greater concentration of Amph CTD ΔSH3 in solution (10 μM) was required to generate fission products of similar curvature to those observed with Amph-FL (100 nM; Fig. 2, D and F). Importantly, the DOGS-NTA-Ni lipids alone did not generate high curvature vesicles before protein exposure (Fig. 3 B, top histogram). Moreover, isolated 6his tags were not found to drive membrane remodeling (Fig. S2 I).

Membrane binding experiments with fluorescently labeled Amph CTD ΔSH3 showed that when 10 μM of protein was present in solution, the protein covered ∼40% of the membrane surface (Fig. 3 D and Fig. S2, J–L). At this coverage, steric pressure from protein crowding is expected to be sufficient to overcome the energetic barrier to membrane fission (Snead et al., 2017). Therefore, the requirement for a high solution concentration of Amph CTD ΔSH3 reflects the conditions necessary to promote crowded binding to the membrane surface. In contrast, Amph-FL showed substantially stronger binding compared with Amph CTD ΔSH3 (Fig. 3 D), likely owing to polymerization of the BAR scaffold, which enables multivalent membrane binding (Sorre et al., 2012; Simunovic et al., 2016). However, plotting membrane vesiculation by Amph CTD ΔSH3 and Amph-FL together as a function of

the coverage of the membrane surface by proteins revealed that data for the two proteins fall along a similar trend (Fig. 3 E). This finding suggests that the requirement for a high concentration of Amph CTD ΔSH3 to drive membrane vesiculation arises primarily from weaker membrane binding in comparison to Amph-FL, rather than from the absence of the N-BAR domain.

A chimera consisting of N-BAR fused to an alternative disordered domain drives fission with similar efficiency to wild-type amphiphysin

Experiments comparing membrane remodeling by Amph-FL and N-BAR imply that assembly of the N-BAR scaffold at the membrane surface facilitates local crowding of the bulky disordered domains in Amph-FL. This reasoning implies that any bulky disordered domain that is brought to the membrane surface by a BAR scaffold should be capable of driving membrane fission. To test this prediction, we created a chimera consisting of the amphiphysin N-BAR domain fused to the C-terminal disordered domain of rat epsin1 (N-BAR-epsin CTD; Fig. 3 F). Importantly, the disordered domain of epsin1 is comparable to the disordered domain of amphiphysin in terms of length (432 versus 383 amino acids, respectively) as well as hydrodynamic radius (Busch et al., 2015). Tethered vesicle fission experiments revealed that N-BAR-epsin CTD generated highly curved fission products from vesicles with an initial average diameter of 200 nm within a similar range of protein concentrations to Amph-FL (Fig. 3 G; compare to Fig. 2 D). Further, both N-BAR-epsin CTD and Amph-FL produced a very similar fraction of fission products with diameters below 45 nm at equivalent concentrations in solution (Fig. 3 H). Finally, SUPER template membrane shedding experiments revealed that in the concentration range of 50–1,000 nM, N-BAR-epsin CTD drove greater membrane release compared with the isolated N-BAR domain (Fig. 3 I), similar to the results of SUPER template experiments comparing N-BAR and Amph-FL (Fig. 1 F). Importantly, the isolated disordered domain of epsin showed no detectable binding to membranes used in fission studies (Fig. S2 D), suggesting that the disordered domain did not enhance membrane recruitment. These findings illustrate the ability of N-BAR scaffolds to promote membrane fission by crowding arbitrary disordered domains at membrane surfaces.

How does crowding among disordered domains overcome the ability of BAR scaffolds to stabilize lipid tubules? One explanation is that steric pressure among the bulky disordered domains of Amph-FL inhibits the assembly of a long-range N-BAR scaffold, which, if allowed to form, would inhibit fission. In support of this hypothesis, when Amph-FL reached ∼70% surface coverage as shown above (Fig. 2 H), the underlying N-BAR domain covered only ∼14% of the membrane, based on membrane footprints for Amph-FL and N-BAR of 79 and 16.5 nm^2 per monomer, respectively (see Materials and methods). This coverage is significantly lower than expected for a fully assembled N-BAR scaffold, which approaches complete coverage (Mim et al., 2012; Adam et al., 2015). Furthermore, the volume available per amphiphysin disordered domain above the N-BAR scaffold is only ∼50% of the volume that each domain would be expected to occupy in solution, based on its radius of gyration (Fig. 3 J; see calculation in Materials and methods). Notably, this calculation assumes that the disordered domains are incompressible, demonstrating that they would have to compress substantially in order to fit around the scaffold. Previous work has shown that substantial compression of disordered domains is energetically costly, likely exceeding the cost of membrane deformation (Busch et al., 2015). Collectively, these arguments suggest that the presence of amphiphysin's bulky disordered domains inhibits assembly of long-range N-BAR scaffolds.

Interestingly, previous structural studies using cryo-EM have reported limited observations of tubular N-BAR scaffolds formed from Amph-FL (Mim et al., 2012; Adam et al., 2015). These structures have been observed on membrane substrates containing a majority of negatively charged lipids, which are thought to provide a strong electrostatic driving force for scaffold assembly (Mim et al., 2012; Adam et al., 2015). Therefore, we performed tethered vesicle fission experiments using a similar membrane composition (Fig. S3). Here, the onset of membrane fission occurred at somewhat higher Amph-FL concentration, 350 nM (Fig. S3) in comparison to 75 nM (Fig. 2, B–F). These results demonstrate that high concentrations of negatively charged lipids cannot prevent membrane fission as protein concentration increases. Indeed, the cryo-EM studies cited above suggest that long-range scaffolds assembled from full-length protein were more rare (Mim et al., 2012). Moreover, these studies employed buffers that lacked small monovalent ions (Mim et al., 2012; Adam et al., 2015), conditions known to favor extension of disordered domains owing to reduced electrostatic screening (Srinivasan et al., 2014). This environment likely enabled the disordered domains to pack more efficiently around the scaffold, in line with the needle-like densities seen protruding from the N-BAR scaffold (Adam et al., 2015).

Disordered domains inhibit tubule formation by BAR scaffolds in live cells

We next sought to evaluate the influence of disordered domains on the membrane remodeling behavior of BAR domains in live mammalian cells. Multiple previous studies have established that overexpression of BAR domains leads to formation of lipid tubules in the cytosol that are coated by BAR scaffolds (Peter et al., 2004; Frost et al., 2008; Boucrot et al., 2012; McDonald et al., 2015). We first replicated these findings by overexpressing the N-BAR domain of human amphiphysin tagged with mCherry (Fig. 4 A) in retinal pigmented epithelial (RPE) cells. We found that N-BAR generated a dense network of tubules inside the cells (Fig. 4 B), in agreement with previous findings (Peter et al., 2004). The number of tubules per cell increased with the expression level of N-BAR (Fig. 4 C), and colocalized with a plasma membrane stain (Fig. S4 A), indicating that many of the tubules originated from the plasma membrane as previously observed (McDonald et al., 2015, 2016). In contrast, overexpression of Amph-FL tagged with mCherry (Fig. 4 A) led to significantly fewer tubules per cell compared with N-BAR (Fig. 4, B–D), suggesting that the disordered domain of Amph-FL inhibited tubule formation. Notably, Amph-FL interacts with the clathrin adaptor network and may therefore recruit other membrane remodeling proteins. As such, it is unclear whether the lack of stable tubules in Amph-FL–expressing cells arose from the disordered domain or from other

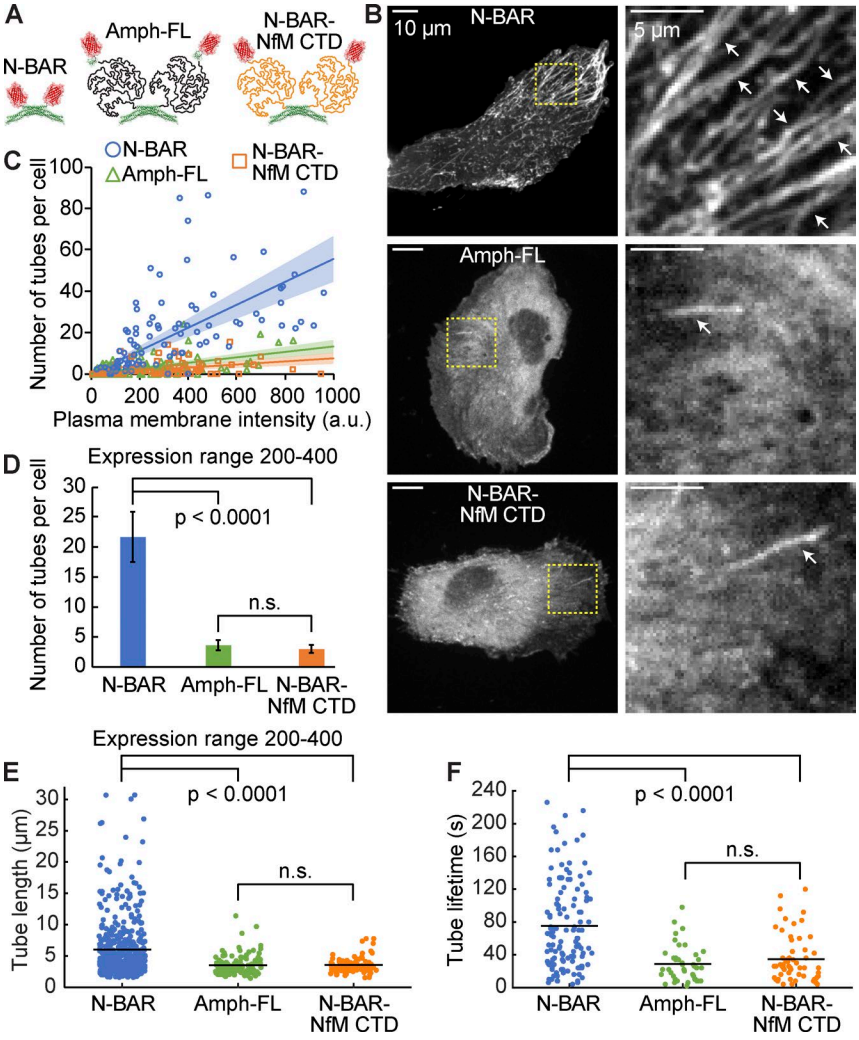

Figure 4. **Disordered domains disrupt N-BAR mediated membrane tubulation in live cells. (A)** Schematic of mCherry (PDB 2H5Q) fusion constructs expressed in cells. **(B)** Confocal images of RPE cells expressing N-BAR (top), Amph-FL (middle), and N-BAR-NfM CTD (bottom). Yellow dashed boxes indicate zoomed regions to the right. White arrows indicate tubules. All cells are within the same range of protein expression level used for quantification in D and E. **(C)** Number of tubes per cell as a function of protein expression level, quantified as the background-subtracted protein intensity at the plasma membrane (see Materials and methods). Lines indicate linear regression with y-intercept set to 0. Shaded regions indicate 99% CI. Line color matches the respective marker color. $n > 90$ cells per condition from two independent transfections. **(D)** Number of tubes per cell within the expression level range of 200–400 brightness units. Bars indicate mean ± SEM; $n > 20$ cells per condition. **(E)** Length of tubes in cells within the expression level range of 200–400 brightness units. Points indicate data; black lines indicate means. $n > 80$ tubes per condition. **(F)** Lifetime of tubes in cells measured from time-lapse total internal reflection fluorescence (TIRF) microscopy videos (see Materials and methods). Points indicate data; black lines indicate means. $n > 40$ tubes per condition. All P values: two-tailed, unpaired Student's *t* tests. (B) Bars, 10 µm; insets, 5 µm. See also Fig. S4 and Video 6.

binding partners recruited by Amph-FL. To distinguish between these possibilities, we created a chimera of N-BAR fused to an alternative disordered domain, from the neuronal protein neurofilament-M (N-BAR-NfM CTD), tagged with mCherry (Fig. 4 A). The disordered C-terminal domain of neurofilament-M acts as an entropic brush, radiating outward along the length of neurofilaments and sterically repelling neighboring disordered domains to control axon diameter (Brown and Hoh, 1997; Kumar et al., 2002). The neurofilament-M disordered domain is similar in length to that of amphiphysin (438 versus 383 amino acids, respectively) but is not involved in endocytosis and therefore contains no binding domains for endocytic proteins. Overexpressing N-BAR-NfM CTD in RPE cells resulted in a similar phenotype to Amph-FL, in which the number of tubules per cell was significantly reduced compared with the isolated N-BAR domain (Fig. 4, B–D). We reach similar conclusions whether protein expression level is matched in terms of the fluorescent protein intensity at the plasma membrane (Fig. 4 C) or in the cytosol (Fig. S4 B). However, the disordered domains of Amph-FL and N-BAR-epsin CTD appeared to reduce plasma membrane binding slightly (Fig. S4 C). Furthermore, while tubules in N-BAR–expressing cells had an average length of 6.0 ± 0.2 µm SEM, tubule lengths in cells expressing Amph-FL and N-BAR-NfM CTD were significantly shorter, 3.5 ± 0.1 and 3.6 ± 0.1 µm SEM, respectively (Fig. 4 E).

Time-lapse imaging of live cells revealed that the tubules formed by Amph-FL and N-BAR-NfM CTD were more transient in comparison to isolated N-BAR (Fig. 4 F and Video 6). Specifically, the tubules in cells expressing N-BAR had an average lifetime of ~75 ± 5 s SEM, whereas tubule lifetime was significantly shorter in cells expressing Amph-FL and N-BAR-NfM CTD, ~29 ± 3 and 35 ± 4 s SEM, respectively (Fig. 4 F). The tubules formed by N-BAR also had greater fluorescence intensity in the protein channel relative to the local background in comparison to Amph-FL and N-BAR-NfM CTD (Fig. S4, D and E). This finding indicates that the disordered domains of Amph-FL and N-BAR-NfM CTD did not promote tubule fission by enhancing protein binding to the membrane surface. Collectively, results from experiments in live cells indicate that bulky disordered domains are capable of disrupting the formation of stable tubules scaffolded by BAR domains, similar to observations in vitro (Fig. 1, C and D). The disordered domains may have inhibited tubule formation in these experiments by driving membrane fission, though future work is needed to test whether steric pressure from disordered domain crowding plays a substantial role in physiological fission events.

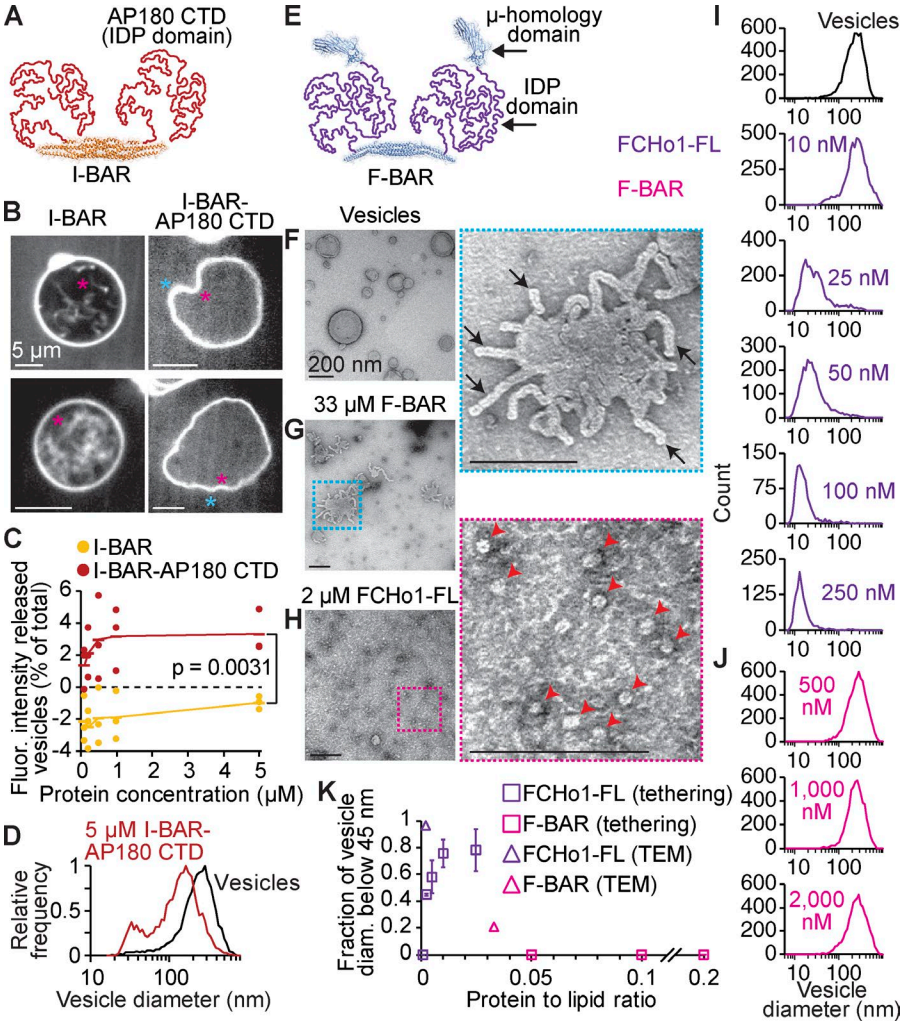

Figure 5. **Disordered domain crowding opposes inverted membrane bending by I-BARs and promotes membrane fission by F-BARs.** GUV membrane composition: 79.5 mol% DOPC, 5 mol% PtdIns(4,5)P_2, 15 mol% DOPS, and 0.5 mol% Oregon Green 488–DHPE. SUPER template membrane composition: 79 mol% DOPC, 5 mol% PtdIns(4,5)P_2, 15 mol% DOPS, and 1 mol% Texas Red–DHPE. Tethered vesicle membrane composition: 76 mol% DOPC, 5 mol% PtdIns(4,5)P_2, 15 mol% DOPS, 2 mol% Oregon Green 488–DHPE, and 2 mol% DP-EG10-biotin. Membrane composition for vesicles in TEM: 80 mol% DOPC, 5 mol% PtdIns(4,5)P_2, and 15 mol% DOPS. **(A)** Schematic of I-BAR-AP180 CTD chimera dimer. IRSp53 I-BAR domain: PDB 1Y2O. **(B)** Two representative confocal micrographs of GUVs after exposure to I-BAR or I-BAR-AP180 CTD. Asterisks indicate direction of membrane bending (magenta: inward; cyan: outward). Fluorescence signal comes from Atto 594–labeled protein. **(C)** SUPER template membrane release comparing I-BAR and I-BAR-AP180 CTD. Dots indicate data and lines indicate mean; n = 3 independent experiments. P value: one-tailed, unpaired Student's t test. **(D)** Tethered vesicle fission experiments reveal that 5 µM I-BAR-AP180 CTD generates highly curved fission vesicles. **(E)** Schematic of FCHo1-FL dimer. F-BAR domain: PDB 2V0O. µ-Homology domain: PDB 5JP2, chain A. (**F–H**) Negative stain TEM micrographs of 200 nm extruded vesicles before exposure to protein (F), after exposure to 33 µM F-BAR (G), and after exposure to 2 µM FCHo1-FL (H). Dashed boxes indicate zoomed regions to the right. Black arrows indicate membrane tubules; red arrowheads indicate fission vesicles. **(I)** Tethered vesicle fission experiments reveal FCHo1-FL generates highly curved fission products over the concentration range of 10–250 nM. **(J)** F-BAR does not drive fission in tethered vesicle fission experiments, even at concentrations up to 2,000 nM. **(K)** Summary of tethered vesicle and TEM experiments, expressed as the proportion of vesicle diameters within the high curvature group of 45 nm or smaller (compare to Fig. 2 F). Markers for tethered vesicle data represent mean ± first SD; n = 3 independent experiments. TEM data from Fig. S5 D. (B) Bars, 5 µm. (F–H) Bars, including insets, 200 nm. See also Fig. S5 and Videos 7 and 8.

Crowding among disordered domains opposes the ability of I-BAR scaffolds to drive inward membrane bending

We next asked how the membrane remodeling ability of crowded disordered domains compares with that of BAR scaffolds. To make this comparison, we created a chimeric protein that places the two mechanisms in direct competition within the same molecule. Specifically, we fused the I-BAR domain of human IRSp53 to the bulky, C-terminal disordered domain of rat AP180 (569 disordered amino acids) to form I-BAR-AP180 CTD (Fig. 5 A). While the I-BAR domain is known to generate inverted membrane curvature (Mattila et al., 2007; Saarikangas et al., 2009), the attached disordered domains should generate steric pressure that will tend to bend the membrane in the opposite direction. Exposing GUVs to the I-BAR domain alone drove inverted membrane tubulation, as expected (Fig. 5 B, left; and Video 7). In contrast, the I-BAR-AP180 CTD chimera drove neither inward nor outward tubulation. Instead, the protein caused the GUV membrane to fluctuate dynamically through nonspherical shapes in which regions of gentle membrane curvature extending both inward and outward were apparent (Fig. 5 B, right; and Video 8). These "frustrated" fluctuations demonstrate that the disordered domain effectively neutralized the ability of the I-BAR domain to drive inward membrane bending. This result suggests that crowding among disordered domains and scaffolding by BAR domains make comparable contributions to membrane remodeling.

Membrane release experiments using SUPER templates showed that exposure to the I-BAR domain (100 nM–5 µM) decreased the amount of membrane shedding to levels lower than the amount of nonspecific shedding that occurred in protein-free buffer (Fig. 5 C, negative values). This result suggests that assembly of the I-BAR scaffold stabilized the membrane against shedding. In contrast, I-BAR-AP180 CTD drove positive membrane release at all concentrations (Fig. 5 C), demonstrating that the disordered domain of AP180 is capable of disrupting the membrane-stabilizing effect of I-BAR. Interestingly, tethered vesicle fission experiments revealed that the highest concentration of I-BAR-AP180 CTD that we tested, 5 µM, drove membrane fission, generating a population of vesicles centered near 30 nm

diameter (Fig. 5 D). This result demonstrates that, under appropriate conditions, steric pressure among crowded disordered domains is sufficient to overcome the structure-based curvature preference of the I-BAR scaffold. Importantly, while wild-type IRSp53 does not naturally contain a large disordered domain, the I-BAR domain–containing proteins MIM and ABBA do contain regions of substantial disorder (~475 amino acids in MIM; Lee et al., 2007). Therefore, our observations raise the question of whether the presumed role of these proteins in driving cellular membrane protrusions can be justified on the basis of in vitro studies of their isolated I-BAR domains (Mattila et al., 2007; Saarikangas et al., 2009).

An F-BAR scaffold drives fission by locally crowding bulky disordered domains

If BAR scaffolds drive membrane fission by concentrating large disordered domains at membrane surfaces, then the ability of Amph-FL to drive fission (Figs. 1 and 2) should extend to other proteins that contain both BAR domains and substantial regions of intrinsic disorder. Interestingly, many proteins that contain the modestly curved F-BAR domain also have this architecture (Roberts-Galbraith and Gould, 2010), including the endocytic proteins FCHo1/2 (Henne et al., 2010), its yeast homologue Syp1 (Reider et al., 2009), the srGAP proteins involved in neuronal development (Wuertenberger and Groemping, 2015), the cytokinesis proteins Cdc15 (Roberts-Galbraith et al., 2010) and Imp2 (McDonald et al., 2016) in *Schizosaccharomyces pombe,* and Hof1 (Meitinger et al., 2011) in *Saccharomyces cerevisiae*. To test this idea, we examined FCHo1 (*Caenorhabditis elegans*), which consists of an N-terminal F-BAR domain followed by an intrinsically disordered domain of 412 amino acids and a C-terminal μ-homology domain (Henne et al., 2010; Umasankar et al., 2014; Ma et al., 2016; Wang et al., 2016; Fig. 5 E). Negative stain TEM revealed that exposure of vesicles with an initial average diameter of 200 nm to the F-BAR domain of FCHo1 drove formation of lipid tubules with an average diameter of 21 ± 2 nm SD (Fig. 5, F and G; and Fig. S5, A and B), in agreement with previous findings (Henne et al., 2007, 2010). In contrast, full-length FCHo1 (FCHo1-FL) did not generate lipid tubules, but instead divided the 200-nm-diameter vesicles into a population of highly curved vesicles with average diameter 17 ± 7 nm SD (Fig. 5 H and Fig. S5, C and D). F-BAR also generated a population of high curvature vesicles in TEM experiments (Fig. S5 D); however, such vesicles accounted for only 20% of the overall distribution, while they accounted for 96% of the vesicle population after exposure to FCHo1-FL at a substantially lower protein-to-lipid ratio (1:30 versus 1:500 for F-BAR and FCHo1-FL, respectively; Fig. 5 K).

Similarly, tethered vesicle fission experiments revealed that FCHo1-FL drove potent membrane fission over the concentration range of 10–250 nM (Fig. 5, I and K), a comparable range to Amph-FL (50–150 nM; Fig. 2, D and F), with a mean diameter of 19 ± 1 nm SEM at 250 nM of FCHo1-FL. However, the F-BAR domain alone did not drive fission in these experiments, even at substantially higher concentrations up to 2 μM (Fig. 5, J and K). Interestingly, in both tethered vesicle and TEM experiments, the fission products of FCHo1-FL had a peak diameter of slightly less than 20 nm, with some vesicles as small as 10 nm. These small diameters suggest that FCHo1-FL may stabilize the formation of membrane micelles, which are similar in morphology to the hemifusion intermediates that form during membrane fission (Campelo and Malhotra, 2012; Frolov et al., 2015). Notably, vesicles in these experiments were composed primarily of the lipid 1,2-dioleoyl-sn-glycero-3-phosphocholine (DOPC), which has a lower bending rigidity than physiological membranes (Dimova, 2014). In contrast, when we increased bilayer rigidity by replacing DOPC with the substantially more rigid, fully saturated lipid 1,2-dipalmitoyl-sn-glycero-3-phosphocholine (DPPC; Lee et al., 2001; Dimova, 2014), the average diameter of fission products increased to ~50 nm at 50 nM of FCHo1-FL, consistent with bilayer vesicles (Fig. S5, E–G). Collectively, these studies show that, despite their gentle curvature, F-BAR scaffolds are also capable of collaborating with disordered domain crowding to drive efficient membrane fission, producing highly curved vesicles. These findings suggest that the ability of BAR domains to assemble into scaffolds that concentrate disordered domains, regardless of their intrinsic structural curvature, makes an important contribution to membrane fission.

Discussion

Here we report that membrane scaffolding by BAR domains works synergistically with steric pressure among bulky disordered domains to drive membrane fission. By highlighting the ability of BAR scaffolds to locally concentrate disordered domains, this work helps to explain how steric pressure can be generated and locally sustained at membrane surfaces. Further, our findings are in contrast with the established view that BAR scaffolds prevent fission by stabilizing membrane tubes (Boucrot et al., 2012). Instead, our work suggests that BAR proteins that contain substantial disordered regions may be drivers of membrane fission. Importantly, previous reports have observed that Amph-FL generates lipid tubules shortly after protein exposure (Takei et al., 1999; Neumann and Schmid, 2013), in agreement with the findings of our experiments with GUVs at early time points (Fig. S1 A). However, we found that at later time points, Amph-FL drove membrane fission in each of our assays (Fig. S1 A and Figs. 1 D and 2 D).

Importantly, our in vitro studies do not fully explain the mechanisms by which proteins drive membrane fission in live cells. However, previous studies in live cells suggest that amphiphysin could be playing a supporting role in membrane fission, potentially via a protein crowding mechanism. For example, deletion of the yeast amphiphysins Rvs161/167 leads to a defect in the entry of clathrin-coated pits into cells (Kaksonen et al., 2005; Kishimoto et al., 2011), suggesting that Rvs161/167 may support membrane fission. However, Rvs161/167 is a heterodimer, and only Rvs167 contains a large disordered domain (Ren et al., 2006). Additionally, depletion of amphiphysin by RNA interference inhibits clathrin-mediated endocytosis in mammalian cells (Meinecke et al., 2013), although this endocytic defect has been previously attributed to a reduction in dynamin recruitment.

Our finding that modestly curved F-BAR domains can also collaborate with bulky disordered domains to drive potent fission is surprising, as it suggests that proteins such as FCHo1/2 may

participate in membrane shaping throughout the maturation of clathrin-coated pits, and may even help drive the final fission event. This hypothesis is in contrast to the idea that FCHo1/2 are primarily involved in the initiation of clathrin-coated pits (Henne et al., 2010; Ma et al., 2016). However, previous work showed that FCHo2 is present throughout the lifetime of clathrin-coated pits (Taylor et al., 2011), supporting the possible role of FCHo2 in membrane shaping. Moreover, many F-BAR proteins involved in other cellular pathways such as cytokinesis also contain large regions of intrinsic disorder (Roberts-Galbraith et al., 2010; Meitinger et al., 2011; McDonald et al., 2016). As such, our findings raise the question of whether F-BAR scaffolds facilitate membrane fission in a variety of contexts beyond membrane traffic.

More broadly, our work raises the possibility that protein assemblies beyond BAR domains may serve as scaffolds for crowding bulky disordered domains in order to ensure efficient membrane fission. One potential example is dynamin, a scaffold-forming GTPase involved in fission of clathrin-coated pits (Antonny et al., 2016). Dynamin plays an essential role in driving membrane fission in diverse cellular contexts (Ramachandran and Schmid, 2018). While dynamin itself does not contain substantial regions of disorder, it assembles with proteins that contain such domains, including amphiphysin and SNX9 (Daumke et al., 2014). We speculate that once recruited by dynamin, these proteins may generate significant steric pressure at membrane necks. In line with this thinking, the yeast dynamin homologue, Vps1, is dispensable for fission, but is necessary for proper localization and accumulation of amphiphysin at clathrin-coated pits (Smaczynska-de Rooij et al., 2010; Kishimoto et al., 2011). A function of Vps1 could therefore be to organize and concentrate bulky disordered domains at membrane necks to promote fission. Moreover, previous studies found that amphiphysin acts synergistically with dynamin to enhance membrane fission (Meinecke et al., 2013; Neumann and Schmid, 2013). However, one report found that amphiphysin alone did not drive membrane fission in the absence of dynamin (Meinecke et al., 2013), in contrast with our findings. Notably, this study used rat amphiphysin 2–6 (Meinecke et al., 2013), a splice variant that contains a disordered domain that is only 30% of the length of the disordered domain in human amphiphysin used in our study (Wigge et al., 1997). The substantially shorter disordered domain likely generates lower steric pressure, which may explain its reduced capacity for membrane vesiculation.

Notably, our results apply specifically to BAR domain proteins that contain bulky disordered regions, while other BAR proteins with shorter disordered domains shape membranes using other mechanisms (Simunovic et al., 2017). The lengths of disordered domains found in BAR domain–containing proteins vary widely (Roberts-Galbraith and Gould, 2010; Salzer et al., 2017), from ∼50 to 400 amino acids in N-BAR–containing proteins (Pietrosemoli et al., 2013). Similarly, the lengths of disordered regions in F-BAR–containing proteins span from less than 100 amino acids in PSTPIP2 (Roberts-Galbraith and Gould, 2010) to greater than 400 in FCHo1 (Pietrosemoli et al., 2013), while in I-BAR–containing proteins, disordered domains span from less than 200 amino acids in IRSp53 (Heung et al., 2008) to greater than 400 in MIM/ABBA (Lee et al., 2007). Future work is needed to better understand the minimal length for which a disordered domain will make a significant contribution to membrane remodeling.

Recent work revealed that endophilin, which contains a BAR domain but lacks a bulky disordered region, promotes membrane fission by acting as a diffusion barrier to lipids (Renard et al., 2015; Simunovic et al., 2017). This friction-driven scission mechanism may be responsible for fission in a clathrin-independent endocytic pathway (Renard et al., 2015; Simunovic et al., 2017). While friction-driven scission and disordered domain crowding are distinct mechanisms, they are not mutually exclusive and may work together to drive fission of endocytic structures. Future work is needed to better understand the potential collaboration between these BAR domain–mediated fission mechanisms.

Our work reveals a synergistic relationship between structured protein assemblies and disordered pressure generators, which can be harnessed to drive membrane fission. It is increasingly recognized that structural disorder is prevalent in membrane trafficking, and that disordered domains are often coupled to structured domains within the same protein molecules (Pietrosemoli et al., 2013). While previous work has focused primarily on structure–function relationships revealed by studying individual protein domains, our findings highlight the importance of examining the collective contributions from both structure and disorder to understand how proteins shape membranes in diverse cellular contexts.

Materials and methods

Chemical reagents

MOPS, Hepes, Tris hydrochloride, NaCl, DTT, IPTG, β-mercaptoethanol, thrombin protease, and Triton X-100 were purchased from Thermo Fisher Scientific. EDTA, EGTA, tris(2-carboxyethyl) phosphine hydrochloride (TCEP), PMSF, EDTA-free protease inhibitor tablets, Thrombin CleanCleave Kit, poly-L-lysine (PLL), Atto 488 NHS-ester, and Atto 594 NHS-ester were purchased from Sigma-Aldrich. Human rhinovirus-3C (HRV-3C) protease, neutravidin, Oregon Green 488–DHPE, and Texas Red–DHPE were purchased from Thermo Fisher Scientific. mPEG–succinimidyl valerate (SVA), biotin-PEG-SVA, mPEG-silane, and biotin-PEG-silane (all PEGs were molecular weight 5,000 D) were purchased from Laysan Bio. Dipalmitoyl-decaethylene glycol-biotin (DP-EG10-biotin) was provided by D. Sasaki of Sandia National Laboratories, Livermore, CA (Momin et al., 2015). All other lipids were purchased from Avanti Polar Lipids, including L-α-phosphatidylinositol-4,5-bisphosphate (PtdIns(4,5)P_2; from porcine brain), DOGS-NTA-Ni, DOPC, and 1,2-dioleoyl-sn-glycero-3-phospho-L-serine (DOPS; sodium salt). The lipid compositions for all experiments are listed in the figure captions.

Plasmids

The pGex6P bacterial expression vector containing full-length human amphiphysin (residues 2–695) was provided by the Baumgart laboratory, University of Pennsylvania, Philadelphia, PA. The N-BAR domain of human amphiphysin (residues 2–242) was cloned into the pGex4T2 bacterial expression vector using BamHI and EcoRI restriction sites. The C-terminal domain of human amphiphysin lacking the SH3 domain (Amph CTD ΔSH3,

residues 240–622) with N-terminal GST and 6his tags was cloned using a previously generated plasmid template, GST-6his-AP180 CTD in pGex4T2 (Busch et al., 2015). AP180 CTD was excised from the template using SalI and XhoI restriction sites, and the Amph CTD ΔSH3 insert was ligated in using the same SalI and XhoI sites. The N-BAR domain of human amphiphysin fused to the C-terminal domain of rat epsin1 (N-BAR-epsin CTD, residues 144–575 of rat epsin1) was cloned by first ligating the N-BAR domain of human amphiphysin (residues 2–242) into pGex4T2 using BamHI and EcoRI restriction sites. Epsin CTD was then ligated in frame with N-BAR using SalI and NotI restriction sites. The I-BAR domain of human IRSp53 (residues 1–250) was cloned by using site-directed mutagenesis to introduce a stop codon at residue 251 in the pGex6P2 plasmid containing full-length IRSp53. The I-BAR domain of human IRSp53 fused to the C-terminal domain of rat AP180 (I-BAR-AP180 CTD, residues 328–896 of rat AP180) was cloned by first ligating the I-BAR domain of human IRSp53 (residues 1–250) into pGex4T2 using BamHI and EcoRI restriction sites. AP180 CTD was then ligated in frame with I-BAR using SalI and XhoI restriction sites. The pGex6P1 vector containing full-length *C. elegans* FCHo1 (residues 1–968) was provided by the Audhya laboratory, University of Wisconsin, Madison, WI (Wang et al., 2016). The F-BAR domain of *C. elegans* FCHo1 (residues 1–276) was cloned into the pGex4T2 vector using BamHI and EcoRI restriction sites.

The pCAGEN mammalian expression vector containing the N-BAR domain of human amphiphysin (residues 1–256), tagged at the C terminus with mCherry, was a gift from T. Meyer, Stanford University, Stanford, CA (Addgene plasmid 85130). Full-length human amphiphysin (residues 1–695) was cloned into the pCAGEN vector, in frame with mCherry at the C terminus, by first excising the N-BAR domain from the template using EcoRI and AgeI restriction sites, and then ligating in Amph-FL using the same EcoRI and AgeI restriction sites. The N-BAR domain of human amphiphysin fused to the C-terminal domain of mouse neurofilament-M (N-BAR-NfM CTD, residues 411–848 of mouse neurofilament-M) was cloned by ligating neurofilament-M CTD into the existing N-BAR-mCherry pCAGEN template, between N-BAR and mCherry, using a single AgeI restriction site. The resulting plasmid contained a GPV linker between N-BAR and neurofilament-M CTD and a GPVAT linker between neurofilament-M CTD and mCherry. All plasmids were confirmed by DNA sequencing.

Protein purification

All proteins were expressed as N-terminal GST fusion constructs in BL21 *Escherichia coli* cells following induction with 1 mM IPTG. Amph-FL, N-BAR, Amph CTD ΔSH3, I-BAR, I-BAR-AP180 CTD, and F-BAR were induced at 30°C for 6–8 h. N-BAR-epsin CTD was induced at 16°C for 20 h. FCHo1-FL was induced at 12°C for 24 h. Cells were harvested, and bacteria were lysed using lysis buffer and probe sonication. For FCHo1-FL, lysis buffer was 100 mM sodium phosphate, pH 8.0, 5 mM EDTA, 5 mM DTT, 10% glycerol, 1 mM PMSF, 1% Triton X-100, and 1× Roche protease inhibitor cocktail. For all other proteins, lysis buffer was 500 mM Tris-HCl, pH 8.0, 5 mM EDTA, 10 mM β-mercaptoethanol or 5 mM TCEP, 5% glycerol, 1 mM PMSF, 1% Triton X-100, and 1× Roche or Pierce protease inhibitor cocktail. Proteins were purified from bacterial extracts by incubating with glutathione resin, followed by extensive washing (at least 10× column volumes). Amph-FL, N-BAR, Amph CTD ΔSH3, and F-BAR were cleaved directly from the resin using soluble HRV-3C (Thermo Fisher Scientific) or thrombin (GE Healthcare) proteases overnight at 4°C with rocking. HRV-3C, which contained a GST tag, was removed by passage through a glutathione agarose column. Thrombin was removed with *p*-aminobenzamidine-agarose resin (Sigma-Aldrich). N-BAR-epsin CTD, I-BAR, and I-BAR-AP180 CTD were eluted with 15 mM reduced glutathione in 500 mM Tris-HCl, pH 8.0, 5 mM EDTA, 10 mM β-mercaptoethanol or 5 mM TCEP, 5% glycerol, and 1 mM PMSF buffer. FCHo1-FL was eluted with 15 mM reduced glutathione in 100 mM sodium phosphate, pH 8.0, 5 mM EDTA, 5 mM DTT, 10% glycerol, and 1 mM PMSF buffer. The proteins were concentrated with EMD Millipore Amicon centrifugal filter units, desalted with Zeba Spin Desalting Columns (Thermo Fisher Scientific), and then incubated with the Thrombin CleanCleave Kit (Sigma-Aldrich), soluble HRV-3C, or soluble thrombin overnight at 4°C with rocking. Cleaved GST was removed by passage through a glutathione agarose column. I-BAR-AP180 CTD and N-BAR-epsin CTD were further purified by gel filtration chromatography using a Superose 6 column equilibrated with 20 mM Tris-HCl, pH 8.0, 150 mM NaCl, 1 mM EDTA, 5 mM EGTA, 1 mM PMSF, and 5 mM DTT. All proteins were stored as small aliquots or liquid nitrogen pellets at −80°C. All proteins except FCHo1-FL were stored in glycerol-free buffer, and all experiments were performed in glycerol-free buffer. FCHo1-FL was stored in the presence of 10 vol% glycerol to improve protein stability, but dilutions during experiments reduced the glycerol concentration to 0.1 vol% or less, which is not expected to affect membrane properties (Pocivavsek et al., 2011).

Protein labeling

Proteins were labeled using amine-reactive, NHS ester-functionalized dyes (Atto-Tec) in 25 mM Hepes, pH 7.35, 150 mM NaCl, and 5 mM TCEP buffer. The concentration of dye was adjusted experimentally to obtain the desired labeling ratio of 0.5–1 dye molecules per protein, typically 2–5 times molar excess of dye. Reactions were performed for 20–30 min at room temperature, and labeled protein was separated from unconjugated dye using Princeton CentriSpin-20 size exclusion spin columns (Princeton Separations).

TEM

Vesicles for EM were composed of 5 mol% PtdIns(4,5)P_2, 15 mol% DOPS, and 80 mol% DOPC. Dried lipid films were hydrated in 20 mM MOPS, pH 7.35, 150 mM NaCl, 0.5 mM EGTA, and EDTA buffer and extruded though a 200-nm pore filter (Whatman). Proteins were diluted to the indicated concentrations in the same MOPS buffer with 5 mM TCEP and incubated with vesicles at 37°C for 30 min (Amph-FL and N-BAR) or 60 min (FCHo1-FL and F-BAR). The vesicle concentration was 1 mM in experiments with Amph-FL, FCHo1-FL, and F-BAR, and 0.1 mM in experiments with N-BAR and in protein-free controls. 5 µl of the mixture was placed onto a glow-discharged, 300 square mesh, carbon-coated grid and stained with 2% uranyl acetate (Electron Microscopy

Sciences). Images were collected on a Tecnai Spirit BioTwin T12 electron microscope (Tecnai). Vesicle and tubule diameters were measured using ImageJ software.

Fluorescence microscopy

A spinning disc confocal microscope (Zeiss Axio Observer Z1 with Yokagawa CSU-X1M) was used to image GUVs, tethered vesicles, and live RPE cells. Laser wavelengths of 488 and 561 nm were used for excitation. Emission filters were centered at 525 nm with a 50-nm width, and 629 nm with a 62-nm width. A triple-pass dichroic mirror was used: 405/488/561 nm. The microscope objective was a Plan-Apochromat 100×, 1.4 numerical aperture oil immersion objective. Images were collected on a cooled (–70°C) EMCCD iXon3 897 camera (Andor Technology).

GUV preparation

GUVs were prepared according to published protocols (Angelova and Dimitrov, 1986). For experiments with N-BAR and Amph-FL, the lipid mixture was 5 mol% PtdIns(4,5)P_2, 15 mol% DOPS, 79.5 mol% DOPC, and 0.5 mol% Oregon Green 488–DHPE. For experiments with 6his peptide, the lipid mixture was 20 mol% DOGS-NTA-Ni, 79.5 mol% DOPC, and 0.5 mol% Texas Red–DHPE. Lipid mixtures were dried into a film on an indium-tin-oxide–coated glass slide and further dried under vacuum overnight. Electroformation was performed at 55°C in 350 milliosmolar sucrose solution. Vesicles were mixed with protein solution at the specified concentration in 20 mM MOPS, pH 7.35, 150 mM NaCl, and 5 mM TCEP buffer. 0.5 mM EGTA and EDTA were included in the buffer and sucrose solution when working with PtdIns(4,5)P_2-containing vesicles to prevent clustering of PtdIns(4,5)P_2. Prior to mixing, the osmolarity of the GUV solution and experiment buffer was measured using a vapor pressure osmometer (Wescor).

SUPER template preparation

SUPER templates were prepared according to the protocol of Neumann et al. (2013). A lipid mixture of 5 mol% PtdIns(4,5)P_2, 15 mol% DOPS, 1 mol% Texas Red DHPE, and 79 mol% DOPC was mixed in a clean glass test tube, the solvent was evaporated, and the lipid film was further dried under vacuum. The lipid film was hydrated in Milli-Q water, subjected to three freeze-thaw cycles in liquid nitrogen, and extruded through a 100-nm pore filter (Whatman). SUPER templates were made by creating a 100 µl mixture consisting of 200 µM liposomes, 1 M NaCl, and 5 × 10^6 of 2.5 µm m-type silica beads (Corpuscular) in a low-adhesion microcentrifuge tube. The mixture was incubated for 30 min at room temperature and gently agitated periodically. The mixture was washed by adding 1 ml Milli-Q water, gently mixing, and spinning at 300 *g* for 2 min in a swinging bucket rotor to pellet the SUPER templates. 1 ml of supernatant was removed, SUPER templates were resuspended in the remaining 100 µl, and washing was repeated a total of four times. SUPER templates were kept on ice and used within 4 h.

Measurement of SUPER template membrane release

SUPER template membrane shedding experiments were performed according to the protocol of Neumann et al. (2013). 10 µl of SUPER templates were gently pipetted into the top of a 90 µl solution of protein at specified concentrations in 20 mM MOPS, pH 7.35, 150 mM NaCl, 0.5 mM EGTA and EDTA, and 5 mM TCEP buffer. SUPER templates were allowed to slowly settle for 30 min at room temperature without being disturbed. SUPER templates containing unreleased membrane were then sedimented by gentle centrifugation at 300 *g* for 2 min in a swinging bucket rotor. 75 µl of supernatant containing released membrane was collected and mixed in a 96-well plate with Triton X-100 at a final concentration of 0.1% and volume of 100 µl. To measure the total fluorescence of SUPER template membrane, a detergent control consisting of SUPER templates added directly to 0.1% Triton X-100, which solubilized all SUPER template membrane, was run. The fluorescence intensity of released membrane was measured in a plate reader using 590-nm excitation light and an emission filter centered at 620 nm. After subtracting the fluorescence of 0.1% Triton X-100 in buffer alone from all measurements, membrane release was calculated by dividing the fluorescence intensity after protein exposure by the fluorescence intensity of the detergent control. The background level of membrane release in the absence of protein was also measured by incubating SUPER templates in buffer alone. This buffer control was subtracted from all measurements as background.

FCS

Imaging wells for FCS used supported lipid bilayers to passivate the glass surface and prevent protein adsorption. Briefly, a well was created with a silicone gasket on an ultraclean coverslip, and a solution of sonicated DOPC vesicles at 1 mM lipid was added. The supported lipid bilayer was formed for 10 min and thoroughly washed in experiment buffer of 50 mM Tris, pH 8.0, 10 mM $CaCl_2$, 150 mm NaCl, 15 mM EGTA, 5 mM EDTA, and 5 mM TCEP. Atto 488–labeled proteins were diluted in experiment buffer and added to the imaging well such that the concentration of Atto 488 dye was ∼1 nM. FCS measurements were acquired on a custom-built time-correlated single photon counting confocal microscope using a 486-nm ps pulsed diode laser. The laser was focused in solution ∼3 µm above the bilayer passivation surface, and fluorescence signal was collected as proteins diffused through the focused laser volume. The signal was split onto separate GaAsP photomultiplier tubes (Hamamatsu) for cross-correlation using Becker and Hickl software. FCS traces were collected for 120 s. The number of FCS traces acquired for Amph CTD ΔSH3, AP180 CTD, and transferrin were 10, 5, and 3, respectively. Each FCS trace was fit with the 2D autocorrelation function:

$$G(t) = \left(1 + a e^{-t/\tau_c}\right) * \left(\frac{C}{1 + \left(t/\tau_D\right)^{\alpha}}\right) + 1,$$

where C is $1/N_p$, N_p is the number of labeled proteins in the focused laser volume, τ_D is the diffusion time, and α is the anomalous diffusion coefficient. a and τ_c, which correct for short time processes such as intersystem crossing, were held constant in the fitting as 0.05 and 5 µs, respectively (Houser et al., 2016). Fitting was performed in Wolfram Mathematica 11 software. α values were between 0.90 and 0.93 for all fits, demonstrating that a substantial correction for anomalous diffusion was not needed.

Fig. S2, E–G, shows representative FCS traces and fits for Amph CTD ΔSH3, AP180 CTD, and transferrin, with mean values of τ_D ± first SD reported next to each trace. The hydrodynamic radius, R_H, of each protein is also reported next to each trace. AP180 CTD was used as a calibration standard to compute R_H of Amph CTD ΔSH3, as τ_D is directly proportional to R_H. AP180 CTD is a disordered protein with a radius that has been well-characterized (Kalthoff et al., 2002; Busch et al., 2015), making it an appropriate calibration standard. This calibration approach also yielded a radius for transferrin that was consistent with its expected radius (Hall et al., 2002), confirming the validity of our approach. The radius of Amph CTD ΔSH3 was taken as 5 nm in estimates of membrane coverage by proteins in Figs. 2 H and 3 D. This value was chosen based on previous studies, which found that the radius of gyration of a disordered protein is ∼1.2-fold greater than the hydrodynamic radius (Sherman and Haran, 2006; Hofmann et al., 2012).

Fig. S2 H shows the relative diffusion time, τ_D, of Amph CTD ΔSH3 in 20 mM MOPS, pH 7.35, in varying concentrations of NaCl. Data are plotted as the relative diffusion time compared with the diffusion time at 150 mM NaCl. Diffusion times were corrected for changes in solution viscosity with changing NaCl concentration (Zhang and Han, 1996). Because τ_D is directly proportional to R_H, the increase in τ_D at 10 mM NaCl indicates an increase in R_H, likely owing to reduced charge screening, which expands and extends the disordered protein (Srinivasan et al., 2014). Similarly, the decrease in τ_D at 1 M NaCl indicates a decrease in R_H, owing to enhanced charge screening, which compacts the disordered protein.

Passivating glass coverslips with PEG and PEG-biotin for tethering vesicles

Glass coverslips were passivated by either directly conjugating PEG-silane and biotin-PEG-silane to the glass, or by coating the glass with a layer of PLL conjugated to PEG and biotin-PEG. For the direct silane conjugation, a 0.67% solution of PEG-silane was prepared in anhydrous isopropanol. Biotin-PEG-silane comprised 5% of the total amount of PEG-silane in the solution. The mixture was held in a bath sonicator for 10–15 min to dissolve the PEG. Acetic acid was added to a concentration of 1%, and 50 µl of the reactive mixture was dropped onto a dry, ultraclean coverslip. Another dry, ultraclean coverslip was sandwiched on top, and the slides were incubated at 70°C for 30–60 min. The slides were separated, washed in ultrapure water, and stored dry for later use. Imaging wells were made by placing silicone gaskets onto the glass and hydrating in 20 mM MOPS, pH 7.35, and 150 mM NaCl buffer. Neutravidin was added to the well at a final concentration of 0.2 mg ml^{-1} and incubated for 10 min, and the well was washed repeatedly with MOPS buffer before adding vesicles.

The biotinylated PLL-PEG was made according to a previous protocol (Ruiz-Taylor et al., 2001). Briefly, amine-reactive PEG-SVA and biotin-PEG-SVA was added to a 40 mg ml^{-1} mixture of PLL in 50 mM sodium tetraborate, pH 8.5, at a molar ratio of one PEG per five lysine subunits. PEG-biotin comprised 2% of the total PEG amount. The mixture was stirred continuously for 6 h at room temperature and buffer exchanged into PBS using Centri-Spin size exclusion columns (Princeton Separations). Imaging wells were made by placing silicone gaskets onto ultraclean coverslips. Wells were coated for 20–30 min with biotinylated PLL-PEG diluted tenfold in 20 mM MOPS, pH 7.35, and 150 mM NaCl buffer. After coating, the well was washed repeatedly with MOPS buffer to wash out excess PLL-PEG. Neutravidin was added to the well following the same process as for PEG-silane slides.

Determination of vesicle diameter from measurements of tethered vesicle brightness

Vesicle diameter distributions were measured using an assay developed by the Stamou group (Stamou et al., 2003; Kunding et al., 2008; Hatzakis et al., 2009). Vesicles in experiments with Amph-FL, N-BAR, N-BAR–epsin CTD, I-BAR–AP180 CTD, FCHo1-FL, and F-BAR were composed of 76 mol% DOPC, 15 mol% DOPS, 5 mol% PtdIns(4,5)P_2, 2 mol% DP-EG10-biotin, and 2 mol% Oregon Green 488–DHPE. Vesicles in experiments with Amph CTD ΔSH3 were composed of a similar lipid mixture, with the exception that DOPS and PtdIns(4,5)P_2 were replaced with 20 mol% DOGS-NTA-Ni. Experiments with Amph-FL and N-BAR on highly charged membranes (Fig. S3) used vesicles composed of 68 mol% DOPS, 23 mol% DOPE, 5 mol% cholesterol, 2 mol% DP-EG10-biotin, and 2 mol% Oregon Green 488–DHPE, similar to Mim et al. (2012). Dried lipid films were hydrated in 20 mM MOPS, pH 7.35, and 150 mM NaCl buffer (0.5 mM EGTA and EDTA were included in experiments with PtdIns(4,5)P_2) and extruded to 200 nm.

Fission experiments were performed by mixing vesicles at a concentration of 10 µM with unlabeled protein at specified concentrations in the above MOPS buffer with 5 mM TCEP. The mixture was incubated at 37°C for either 30 min (Amph-FL, N-BAR, Amph CTD ΔSH3, and N-BAR-epsin CTD) or 60 min (I-BAR-AP180 CTD, FCHo1-FL, and F-BAR). During the incubation period, imaging wells were prepared as described above. After incubation, the mixtures were added to the wells and vesicles were allowed to tether for 10 min before washing repeatedly to remove untethered vesicles. Multiple spinning disc confocal z-stacks of tethered vesicles were acquired with a z-step of 0.1 µm. The same laser power and camera gain settings were used for all experiments. Notably, we used spinning disc confocal microscopy rather than TIRF microscopy because the low penetration depth of TIRF microscopy would not evenly illuminate larger vesicles. The greater illumination depth of spinning disc confocal microscopy ensures that vesicles of a broad diameter distribution are evenly illuminated.

All images in the z-stacks were cropped to the center 171 × 171 pixels (center 1/9), and the frame with the greatest mean brightness was selected as the best focus image for analysis. Fluorescence amplitudes of diffraction-limited puncta were obtained using cmeAnalysis particle detection software (Aguet et al., 2013). Individual vesicles were detected by fitting 2D Gaussian profiles to each puncta. The SD of the Gaussian profile was determined from the point spread function of our microscope. The brightness values of detected puncta were reported as valid if they were diffraction-limited and had amplitudes significantly above their local fluorescence background. To further ensure that puncta were well above the noise threshold, we only accepted puncta that persisted at the same location through five consecutive imaging frames.

To convert fluorescence brightness values to vesicle diameters, we computed a scaling factor that centered the mean of the vesicle brightness distribution of a high-curvature, sonicated vesicle sample to the average diameter of the same vesicles obtained from dynamic light scattering. This scaling factor was then used to scale the vesicle brightness distributions after protein exposure to distributions of vesicle diameter.

Determination of membrane coverage by proteins from measurements of vesicle and protein brightness

Vesicles in experiments with Amph-FL and N-BAR were composed of 76 mol% DOPC, 15 mol% DOPS, 5 mol% PtdIns(4,5)P_2, 2 mol% DP-EG10-biotin, and 2 mol% Oregon Green 488–DHPE. DOPS and PtdIns(4,5)P_2 were replaced with 20 mol% DOGS-NTA-Ni in experiments with Amph CTD ΔSH3. Dried lipid films were hydrated in 20 mM MOPS, pH 7.35, and 150 mM NaCl buffer (0.5 mM EGTA and EDTA were included in experiments with PtdIns(4,5)P_2) and sonicated or extruded to 200 or 30 nm. Imaging wells were prepared as described above. Vesicles were diluted to 5 µM in the wells and allowed to tether for 10 min. Untethered vesicles were removed by thorough washing with MOPS buffer. After tethering, Atto 594–labeled protein was added to the specified concentration, and multiple spinning disc confocal z-stacks of lipid and protein fluorescence were acquired, with a z-step of 0.1 µm. Images were collected after ∼15 min incubation of protein with vesicles. The same laser power and camera gain settings were used for all experiments. Fig. S2 A shows images of tethered vesicles with 10 and 25 nM Amph-FL-Atto 594, demonstrating increased protein brightness (and therefore membrane coverage) with increasing protein concentration.

Images were cropped, and individual vesicle puncta were detected using cmeAnalysis software (Aguet et al., 2013), following a similar approach described in the previous section. Here we only accepted puncta that persisted at the same location through three consecutive imaging frames. The algorithm also searched for fluorescent puncta in the protein channel using the centroids of the detected fluorescent puncta in the master lipid channel. The search region in the protein channel was three times the SD of the Gaussian fit to the point spread function of our microscope. We estimated vesicle diameters from lipid fluorescence brightnesses by calibrating against dynamic light scattering, as described in the previous section. We estimated the number of bound proteins on each vesicle by comparing brightness values in the protein channel to the brightness of a single molecule of Atto 594–labeled protein. Images of single molecules of Atto 594–labeled proteins were obtained by adding a dilute concentration of protein to an imaging well on an ultraclean coverslip, and imaging single proteins adhered to the coverslip surface in a similar manner as described for the tethered vesicles. A linear correction for camera exposure time was applied to the single molecule brightness, as longer exposure times were required to image single molecules compared with membrane-bound protein. Fig. S2 B shows a plot of the raw protein intensity values as a function of vesicle intensity for 10 and 25 nM Amph-FL. The 25-nM data show a higher slope than 10 nM, indicating greater membrane coverage. Fig. S2 C shows this same data after processing, plotted as the number of membrane-bound proteins as a function of vesicle diameter.

Membrane coverage by proteins was estimated for each vesicle by dividing the area occupied by membrane-bound proteins by the corresponding vesicle surface area. The projected membrane footprints of N-BAR, Amph-FL, and Amph CTD ΔSH3 monomers were assumed to be 16.5 (Adam et al., 2015), 79, and 79 nm^2, respectively. The average membrane coverage was estimated as the mean of all individual vesicle coverage values. To confirm the validity of this analysis approach, we also plotted the area of membrane-bound proteins as a function of vesicle surface area, as shown in Fig. S2 L for the 1 µM Amph CTD ΔSH3 dataset. The slope of a linear fit to these data provides an alternative estimate of membrane coverage. The slope of 0.21, or 21% coverage, agrees well with 24% membrane coverage in Fig. 3 D that was estimated using the method described above.

Data with Amph CTD ΔSH3 in Fig. 3 D were collected using 200-nm–extruded vesicles. However, Amph-FL and N-BAR were found to strongly deform and remodel 200-nm vesicles. Therefore, data with N-BAR and Amph-FL in Fig. 2, G and H were collected using vesicles of higher initial curvature, which were found to not undergo substantial remodeling during experiments. Specifically, N-BAR and Amph-FL data were collected using sonicated and 30-nm–extruded vesicles, respectively. Vesicle diameters were estimated by calibrating against a sample of the same vesicles before protein exposure, with the exception of sonicated vesicles. We found that calibrating against a 30-nm–extruded vesicle sample, made from the same lipid mixture on the same day, provided a reliable estimate of the diameter distribution of sonicated vesicles.

Generation of BFP-tagged clathrin light chain (BFP-CLC) RPE cell line

A plasmid for expression of BFP-CLC was generated by replacing the mCherry domain of mCherry–clathrin light chain (CLC), a gift from T. Kirchhausen, Harvard Medical School, Boston, MA (Addgene 53972). The mCherry fluorophore was removed and replaced with tagBFP, a gift from F. Perez, Institut Curie, Paris, France (Addgene 65257). mCherry was excised from the mCherry-CLC plasmid using AgeI and XhoI restriction enzymes. TagBFP was amplified from the li-Str_ManII-SBP-tagBFP plasmid using PCR primers, which introduced AgeI and XhoI restriction sites. The resulting tagBFP sequence was digested and ligated onto the CLC backbone to generate BFP-CLC with a linker sequence of HKGRPTR. The CLC-BFP construct was then excised using AgeI and EcoRI restriction sites and ligated into a pLJM1 backbone obtained from Addgene as a gift from D. Sabatini, Massachusetts Institute of Technology, Cambridge, MA (Addgene 19319). Once subcloned into this viral transfer plasmid, lentiviruses were generated by transfecting the BFP-CLC construct with the envelope plasmid VSVG (a gift from J. Lippincott-Schwartz, Howard Hughes Medical Institute Janelia Research Campus, Ashburn, VA; Addgene 11912) and packaging plasmid pCMV-dR8.91 (a gift from J. Zoldan, University of Texas at Austin, Austin, TX). Lentiviral particles were then harvested, filtered, and incubated with human RPE recipient cells (ARPE-19, purchased from American Type Culture Collection). Cells were incubated with

2 µg/ml puromycin for 1 wk to select for transduced cells, which were then used to generate the monoclonal cell line stably expressing BFP-CLC.

Cell culture and transfection

BFP-CLC RPE cells were grown in 1:1 F12:DMEM supplemented with 10% FBS, 20 mM Hepes, Pen/Strep/L-glutamine (100 U/ml, 100 µg/ml, and 300 µg/ml, respectively) and incubated at 37°C with 5% CO_2. Cells were seeded onto acid-washed coverslips at a density of 5 × 10^4 cells per coverslip for 24 h before transfection with 1–2 µg of plasmid DNA using 3 µl Fugene transfection reagent per microgram of DNA (Promega). Cells were imaged 16–20 h after transfection. Two independent transfections were performed for each plasmid construct, and data were pooled from both transfections.

Spinning disc confocal z-stacks of BFP-CLC and the mCherry fusion protein were collected with a z-step of 0.25 µm. z-Stacks were analyzed for the number of tubes per cell and tube length. Image analysis was performed using ImageJ software. The plasma membrane frame was chosen by identifying the BFP-CLC frame in which the clathrin-coated structures were best in focus. The plasma membrane expression level of the mCherry fusion protein was then quantified by measuring the mean brightness on a region of the plasma membrane, away from the nucleus and bright structures. Protein expression level was also quantified in the cytosol by measuring the mean brightness of the fluorescent protein 1 µm above the plasma membrane. Membrane tubes were counted at one frame above the plasma membrane frame. Figs. 4 C and S4 B plot the number of tubes per cell as a function of protein expression level at the plasma membrane and in the cytosol, respectively. Tube lengths were quantified as the end-to-end distances of the tubes.

Fig. S4 A shows an image of a cell stained with CellMask Green plasma membrane stain (Thermo Fisher Scientific). Before imaging, the cells were incubated for 5 min at 37°C in a solution of the CellMask Green stain diluted 1,000-fold in sterile PBS. The solution was removed, and the cells were washed three times with media before imaging.

A custom-built TIRF microscope was used to collect time-lapse videos of live cells. A 532-nm laser was used to excite mCherry, and a 635-nm laser was used for autofocus. An Olympus IX73 microscope body was equipped with a Photometrics Evolve Delta EMCCD camera and a Zeiss plan-apochromat 100× 1.46 NA oil immersion TIRF objective. The objective was heated to 37°C using a Pecon TempController 2000–2 objective heater. The emission filter for the 532-nm laser was a dual bandpass filter centered at 583 nm with 37-nm width and 707 nm with 51-nm width, which minimized signal from the autofocus laser. Videos were collected at the plasma membrane just above the coverslip surface in 2-s intervals for 120 frames. Tube lifetimes and intensities were quantified from TIRF videos. Only videos of cells with similar expression level, acquired under identical imaging settings, were used for analysis. For the tube lifetime analysis in Fig. 4 F, only tubes that appeared within the time course of imaging and departed before the end of the time course were included. For the tube intensity analysis, a single frame in the video with the maximum number of tubes was selected, and the average tube intensity was measured along a straight line drawn on the tube. The mean intensity along an identical line on either side of the tube was also measured, and these values were averaged to estimate the local background intensity of the tube. The protein enrichment on the tube was then quantified as the ratio of the tube intensity to the local background, after subtracting the camera noise background from both values.

Statistics and sample sizes

For TEM experiments, vesicle diameter distributions in Fig. 1 E are composed of $n > 400$ vesicles for each condition. Tubule diameter distributions in Fig. S1 C (N-BAR) and Fig. S5 B (F-BAR) are composed of $n > 300$ and $n > 500$ tubules, respectively. Vesicle diameter distributions in Fig. S5 D are composed of $n > 250$ vesicles for each condition. Exact n values are provided in the figure legends.

For SUPER template experiments, markers in Figs. 1 F, S1 E, 3 I, and 5 C represent $n = 3$ independent measurements of SUPER template membrane release at each protein concentration. The indicated P values were calculated using unpaired, one-tailed Student's t tests.

For tethered vesicle fission experiments, vesicle diameter distributions represent data pooled from three independent experiments at each protein concentration. Fig. 2, C–E (Amph-FL and N-BAR), represents $n > 3{,}500$ vesicles for all distributions except 1 and 5 µM Amph-FL, where $n > 300$ vesicles. Fig. 3 B (Amph CTD ΔSH3) represents $n > 4{,}100$. Fig. 3 G (N-BAR-epsin CTD) represents $n > 1{,}000$. Fig. 5 D (I-BAR-AP180 CTD) represents $n > 4{,}800$. Fig. 5, I and J (FCHo1-FL and F-BAR), represents $n > 900$. Fig. S3, B–D (Amph-FL and N-BAR on highly charged vesicles), represents $n > 800$. Fig. S5 E (FCHo1-FL on DPPC vesicles) represents $n > 3{,}900$. Markers in Fig. 2 F; Fig. 3, C and H; Fig. 5 K; Fig. S3 E; and Fig. S5 G show mean ± first SD of the three independent experiments.

For membrane coverage experiments on tethered vesicles, markers in Fig. 2, G and H, show mean ± 95% CI, with $n > 1{,}700$ vesicles at each concentration. Amph CTD ΔSH3 markers in Fig. 3 D show mean ± first SD from three independent experiments, with $n > 2{,}900$ total vesicles at each concentration.

In cell experiments, Fig. 4 C displays data from $n > 90$ cells per condition from two independent transfections. Fig. 4 D displays a subset of the data in Fig. 4 C that is within the specified protein expression range, with $n > 20$ cells per condition. Bars represent mean ± SEM. Fig. 4 E displays the lengths of individual tubes from cells within the specified protein expression range, where $n > 80$ tubes per condition. Fig. 4 F displays the lifetimes of individual tubes measured from TIRF videos, where $n > 40$ tubes per condition. Black lines in Fig. 4, E and F, indicate means. The indicated P values were calculated using unpaired, two-tailed Student's t tests.

Calculation of IDP compression above BAR scaffold

The volume per IDP attached to the BAR scaffold was estimated as the volume of a cylindrical shell surrounding a membrane tube, with thickness equal to twice the radius of gyration of the IDP domains, divided by the number of BAR domains in the

scaffold. The cylindrical shell volume surrounding the membrane tube is therefore

$$V_{shell} = V_o - V_i = \pi L(R_o^2 - R_i^2),$$

where V_o and V_i are the outer and inner radii of the shell, respectively, L is the tube length, R_i is the radius of the membrane tube, and $R_o = R_i + 2r_{IDP}$, with r_{IDP} equal to the radius of gyration of amphiphysin's disordered domain. The number of proteins in the scaffold is

$$n_{prot} = \frac{A_i}{A_{BAR}} = \frac{2\pi R_i L}{A_{BAR}},$$

where A_i is the surface area of the membrane tube and A_{BAR} is the area occupied per BAR monomer. The volume per compressed, scaffold-anchored disordered domain is

$$V_{IDP,compressed} = \frac{V_{shell}}{n_{prot}} = \frac{A_{BAR}(R_o^2 - R_i^2)}{2R_i},$$

and the un-compressed volume of the disordered domain is

$$V_{IDP,un-compressed} = \frac{4}{3}\pi r_{IDP}^3.$$

Parameter values were taken as $A_{BAR} = 16.5$ nm^2, $R_i = 14$ nm (both from Adam et al., 2015), and $r_{IDP} = 5$ nm. Using these values, $V_{IDP,compressed} = 224$ nm^3 and $V_{IDP,un-compressed} = 524$ nm^3, corresponding to an ∼60% compression of the disordered domain volume to accommodate the scaffold geometry. Notably, the cylindrical shell was assumed to have a constant thickness of $2r_{IDP}$, which represents the volume that would be required to accommodate the disordered protein domains if they were incompressible. See also Fig. 3 J.

Online supplemental material

Fig. S1 shows GUV and TEM experiments with N-BAR and Amph-FL, SUPER template experiments comparing Amph-FL and the ENTH domain, and further analysis of tethered vesicle experiments with N-BAR and Amph-FL. Fig. S2 shows membrane coverage experiments using tethered vesicles, FCS of Amph CTD ΔSH3, and GUV-binding experiments with 6his peptide. Fig. S3 shows membrane fission experiments with N-BAR and Amph-FL on highly charged membranes. Fig. S4 shows further analysis of experiments with live RPE cells. Fig. S5 shows TEM and tethered vesicle experiments with F-BAR and FCHo1-FL. Videos 1 and 2 show lipid tubules generated from GUVs by N-BAR and Amph-FL, respectively. Videos 3 and 4 show collapsing of GUVs after exposure to N-BAR and Amph-FL, respectively. Video 5 shows vesiculation of GUVs by Amph-FL. Video 6 shows TIRF microscopy of tubules in live RPE cells. Videos 7 and 8 show GUV membrane remodeling driven by I-BAR and I-BAR-AP180 CTD, respectively.

Acknowledgments

We thank Dr. Carl Hayden for assistance with fluorescence microscopy and FCS experiments. We thank Dr. Anjon Audhya for advice on the purification of FCHo1-FL. We thank Liping Wang, Lafer laboratory, for assistance with protein expression and purification. We thank Dr. Darryl Sasaki for providing DP-EG10-biotin. We thank Dr. Gaudenz Danuser and Dr. Sandra Schmid, University of Texas Southwestern, Dallas, TX, for freely providing cmeAnalysis particle detection software. We thank Dr. Dwight Romanovicz and the Institute for Cellular and Molecular Biology Microscopy Facility at the University of Texas at Austin, Austin, TX, for assistance with EM.

J.C. Stachowiak and E.M. Lafer acknowledge funding from the National Institutes of Health (R01GM112065), including an administrative supplement for diversity in support of W.F. Zeno. W.T. Snead acknowledges the support of a Ruth L. Kirschstein National Research Service Award Predoctoral Fellowship from the National Institutes of Health (F31GM121013), as well as a fellowship from the Graduate School, University of Texas at Austin. G. Kago acknowledges the support of a National Science Foundation Graduate Research Fellowship (DGE-1610403). We acknowledge the support of the University of Texas Health Science Center at San Antonio Center for Macromolecular Interactions, which is supported by the Mays Cancer Center through the National Cancer Institute (P30 grant CA054174), and Texas state funds provided through the Office of the Vice President for Research of the University of Texas Health Science Center at San Antonio.

The authors declare no competing financial interests.

Author contributions: All authors designed and performed experiments, consulted together on the data, and wrote the manuscript.

Submitted: 16 July 2018
Revised: 12 October 2018
Accepted: 8 November 2018

References

Adam, J., N. Basnet, and N. Mizuno. 2015. Structural insights into the cooperative remodeling of membranes by amphiphysin/BIN1. *Sci. Rep.* 5:15452. https://doi.org/10.1038/srep15452

Aguet, F., C.N. Antonescu, M. Mettlen, S.L. Schmid, and G. Danuser. 2013. Advances in analysis of low signal-to-noise images link dynamin and AP2 to the functions of an endocytic checkpoint. *Dev. Cell.* 26:279–291. https://doi.org/10.1016/j.devcel.2013.06.019

Ambroso, M.R., B.G. Hegde, and R. Langen. 2014. Endophilin A1 induces different membrane shapes using a conformational switch that is regulated by phosphorylation. *Proc. Natl. Acad. Sci. USA.* 111:6982–6987. https://doi.org/10.1073/pnas.1402233111

Angelova, M., and D. Dimitrov. 1986. Liposome electroformation. *Faraday Discuss.* 81:303–311. https://doi.org/10.1039/dc9868100303

Antonny, B., C. Burd, P. De Camilli, E. Chen, O. Daumke, K. Faelber, M. Ford, V.A. Frolov, A. Frost, J.E. Hinshaw, et al. 2016. Membrane fission by dynamin: what we know and what we need to know. *EMBO J.* 35:2270–2284. https://doi.org/10.15252/embj.201694613

Bhagatji, P., R. Leventis, J. Comeau, M. Refaei, and J.R. Silvius. 2009. Steric and not structure-specific factors dictate the endocytic mechanism of glycosylphosphatidylinositol-anchored proteins. *J. Cell Biol.* 186:615–628. https://doi.org/10.1083/jcb.200903102

Boucrot, E., A. Pick, G. Çamdere, N. Liska, E. Evergren, H.T. McMahon, and M.M. Kozlov. 2012. Membrane fission is promoted by insertion of amphipathic helices and is restricted by crescent BAR domains. *Cell.* 149:124–136. https://doi.org/10.1016/j.cell.2012.01.047

Brown, H.G., and J.H. Hoh. 1997. Entropic exclusion by neurofilament sidearms: a mechanism for maintaining interfilament spacing. *Biochemistry.* 36:15035–15040. https://doi.org/10.1021/bi9721748

Busch, D.J., J.R. Houser, C.C. Hayden, M.B. Sherman, E.M. Lafer, and J.C. Stachowiak. 2015. Intrinsically disordered proteins drive membrane curvature. *Nat. Commun.* 6:7875. https://doi.org/10.1038/ncomms8875

Campelo, F., and V. Malhotra 2012. Membrane fission: the biogenesis of transport carriers. *Annu. Rev. Biochem.* 81:407–427. https://doi.org/10.1146/annurev-biochem-051710-094912

Conner, S.D., and S.L. Schmid. 2003. Regulated portals of entry into the cell. *Nature.* 422:37–44. https://doi.org/10.1038/nature01451

Copic, A., C.F. Latham, M.A. Horlbeck, J.G. D'Arcangelo, and E.A. Miller. 2012. ER cargo properties specify a requirement for COPII coat rigidity mediated by Sec13p. *Science.* 335:1359–1362. https://doi.org/10.1126/science.1215909

Daumke, O., A. Roux, and V. Haucke. 2014. BAR domain scaffolds in dynamin-mediated membrane fission. *Cell.* 156:882–892. https://doi.org/10.1016/j.cell.2014.02.017

Dimova, R. 2014. Recent developments in the field of bending rigidity measurements on membranes. *Adv. Colloid Interface Sci.* 208:225–234. https://doi.org/10.1016/j.cis.2014.03.003

Di Paolo, G., S. Sankaranarayanan, M.R. Wenk, L. Daniell, E. Perucco, B.J. Caldarone, R. Flavell, M.R. Picciotto, T.A. Ryan, O. Cremona, and P. De Camilli. 2002. Decreased synaptic vesicle recycling efficiency and cognitive deficits in amphiphysin 1 knockout mice. *Neuron.* 33:789–804. https://doi.org/10.1016/S0896-6273(02)00601-3

Ferguson, S.M., A. Raimondi, S. Paradise, H. Shen, K. Mesaki, A. Ferguson, O. Destaing, G. Ko, J. Takasaki, O. Cremona, et al. 2009. Coordinated actions of actin and BAR proteins upstream of dynamin at endocytic clathrin-coated pits. *Dev. Cell.* 17:811–822. https://doi.org/10.1016/j.devcel.2009.11.005

Frolov, V.A., A. Escalada, S.A. Akimov, and A.V. Shnyrova. 2015. Geometry of membrane fission. *Chem. Phys. Lipids.* 185:129–140. https://doi.org/10.1016/j.chemphyslip.2014.07.006

Frost, A., R. Perera, A. Roux, K. Spasov, O. Destaing, E.H. Egelman, P. De Camilli, and V.M. Unger. 2008. Structural basis of membrane invagination by F-BAR domains. *Cell.* 132:807–817. https://doi.org/10.1016/j.cell.2007.12.041

Frost, A., V.M. Unger, and P. De Camilli. 2009. The BAR domain superfamily: membrane-molding macromolecules. *Cell.* 137:191–196. https://doi.org/10.1016/j.cell.2009.04.010

Gallop, J.L., C.C. Jao, H.M. Kent, P.J. Butler, P.R. Evans, R. Langen, and H.T. McMahon. 2006. Mechanism of endophilin N-BAR domain-mediated membrane curvature. *EMBO J.* 25:2898–2910. https://doi.org/10.1038/sj.emboj.7601174

Guerrier, S., J. Coutinho-Budd, T. Sassa, A. Gresset, N.V. Jordan, K. Chen, W.L. Jin, A. Frost, and F. Polleux. 2009. The F-BAR domain of srGAP2 induces membrane protrusions required for neuronal migration and morphogenesis. *Cell.* 138:990–1004. https://doi.org/10.1016/j.cell.2009.06.047

Hall, D.R., J.M. Hadden, G.A. Leonard, S. Bailey, M. Neu, M. Winn, and P.F. Lindley. 2002. The crystal and molecular structures of diferric porcine and rabbit serum transferrins at resolutions of 2.15 and 2.60 A, respectively. *Acta Crystallogr. D Biol. Crystallogr.* 58:70–80. https://doi.org/10.1107/S0907444901017309

Hatzakis, N.S., V.K. Bhatia, J. Larsen, K.L. Madsen, P.Y. Bolinger, A.H. Kunding, J. Castillo, U. Gether, P. Hedegård, and D. Stamou. 2009. How curved membranes recruit amphipathic helices and protein anchoring motifs. *Nat. Chem. Biol.* 5:835–841. https://doi.org/10.1038/nchembio.213

Helfrich, W. 1973. Elastic Properties of Lipid Bilayers - Theory and Possible Experiments. *Z. Naturforsch. C.* 28:693–703.

Henne, W.M., H.M. Kent, M.G. Ford, B.G. Hegde, O. Daumke, P.J. Butler, R. Mittal, R. Langen, P.R. Evans, and H.T. McMahon. 2007. Structure and analysis of FCHo2 F-BAR domain: a dimerizing and membrane recruitment module that effects membrane curvature. *Structure.* 15:839–852. https://doi.org/10.1016/j.str.2007.05.002

Henne, W.M., E. Boucrot, M. Meinecke, E. Evergren, Y. Vallis, R. Mittal, and H.T. McMahon. 2010. FCHo proteins are nucleators of clathrin-mediated endocytosis. *Science.* 328:1281–1284. https://doi.org/10.1126/science.1188462

Heung, M.Y., B. Visegrady, K. Fütterer, and L.M. Machesky. 2008. Identification of the insulin-responsive tyrosine phosphorylation sites on IRSp53. *Eur. J. Cell Biol.* 87:699–708. https://doi.org/10.1016/j.ejcb.2008.02.010

Hofmann, H., A. Soranno, A. Borgia, K. Gast, D. Nettels, and B. Schuler. 2012. Polymer scaling laws of unfolded and intrinsically disordered proteins quantified with single-molecule spectroscopy. *Proc. Natl. Acad. Sci. USA.* 109:16155–16160. https://doi.org/10.1073/pnas.1207719109

Houser, J.R., D.J. Busch, D.R. Bell, B. Li, P. Ren, and J.C. Stachowiak. 2016. The impact of physiological crowding on the diffusivity of membrane bound proteins. *Soft Matter.* 12:2127–2134. https://doi.org/10.1039/C5SM02572A

Hurley, J.H., E. Boura, L.A. Carlson, and B. Różycki. 2010. Membrane budding. *Cell.* 143:875–887. https://doi.org/10.1016/j.cell.2010.11.030

Isas, J.M., M.R. Ambroso, P.B. Hegde, J. Langen, and R. Langen. 2015. Tubulation by amphiphysin requires concentration-dependent switching from wedging to scaffolding. *Structure.* 23:873–881. https://doi.org/10.1016/j.str.2015.02.014

Itoh, T., K.S. Erdmann, A. Roux, B. Habermann, H. Werner, and P. De Camilli. 2005. Dynamin and the actin cytoskeleton cooperatively regulate plasma membrane invagination by BAR and F-BAR proteins. *Dev. Cell.* 9:791–804. https://doi.org/10.1016/j.devcel.2005.11.005

Jiang, Z., M. de Messieres, and J.C. Lee. 2013. Membrane remodeling by α-synuclein and effects on amyloid formation. *J. Am. Chem. Soc.* 135:15970–15973. https://doi.org/10.1021/ja405993r

Kaksonen, M., C.P. Toret, and D.G. Drubin. 2005. A modular design for the clathrin- and actin-mediated endocytosis machinery. *Cell.* 123:305–320. https://doi.org/10.1016/j.cell.2005.09.024

Kalthoff, C., J. Alves, C. Urbanke, R. Knorr, and E.J. Ungewickell. 2002. Unusual structural organization of the endocytic proteins AP180 and epsin 1. *J. Biol. Chem.* 277:8209–8216. https://doi.org/10.1074/jbc.M111587200

Kishimoto, T., Y. Sun, C. Buser, J. Liu, A. Michelot, and D.G. Drubin. 2011. Determinants of endocytic membrane geometry, stability, and scission. *Proc. Natl. Acad. Sci. USA.* 108:E979–E988. https://doi.org/10.1073/pnas.1113413108

Kumar, S., X. Yin, B.D. Trapp, J.H. Hoh, and M.E. Paulaitis. 2002. Relating interactions between neurofilaments to the structure of axonal neurofilament distributions through polymer brush models. *Biophys. J.* 82:2360–2372. https://doi.org/10.1016/S0006-3495(02)75581-1

Kunding, A.H., M.W. Mortensen, S.M. Christensen, and D. Stamou. 2008. A fluorescence-based technique to construct size distributions from single-object measurements: application to the extrusion of lipid vesicles. *Biophys. J.* 95:1176–1188. https://doi.org/10.1529/biophysj.108.128819

Lee, C.H., W.C. Lin, and J. Wang. 2001. All-optical measurements of the bending rigidity of lipid-vesicle membranes across structural phase transitions. *Phys. Rev. E Stat. Nonlin. Soft Matter Phys.* 64:020901. https://doi.org/10.1103/PhysRevE.64.020901

Lee, S.H., F. Kerff, D. Chereau, F. Ferron, A. Klug, and R. Dominguez. 2007. Structural basis for the actin-binding function of missing-in-metastasis. *Structure.* 15:145–155. https://doi.org/10.1016/j.str.2006.12.005

Liu, Y.W., S. Neumann, R. Ramachandran, S.M. Ferguson, T.J. Pucadyil, and S.L. Schmid. 2011. Differential curvature sensing and generating activities of dynamin isoforms provide opportunities for tissue-specific regulation. *Proc. Natl. Acad. Sci. USA.* 108:E234–E242. https://doi.org/10.1073/pnas.1102710108

Ma, L., P.K. Umasankar, A.G. Wrobel, A. Lymar, A.J. McCoy, S.S. Holkar, A. Jha, T. Pradhan-Sundd, S.C. Watkins, D.J. Owen, and L.M. Traub. 2016. Transient Fcho1/2·Eps15/R·AP-2 Nanoclusters Prime the AP-2 Clathrin Adaptor for Cargo Binding. *Dev. Cell.* 37:428–443. https://doi.org/10.1016/j.devcel.2016.05.003

Mattila, P.K., A. Pykäläinen, J. Saarikangas, V.O. Paavilainen, H. Vihinen, E. Jokitalo, and P. Lappalainen. 2007. Missing-in-metastasis and IRSp53 deform PI(4,5)P2-rich membranes by an inverse BAR domain-like mechanism. *J. Cell Biol.* 176:953–964. https://doi.org/10.1083/jcb.200609176

McDonald, N.A., C.W. Vander Kooi, M.D. Ohi, and K.L. Gould. 2015. Oligomerization but Not Membrane Bending Underlies the Function of Certain F-BAR Proteins in Cell Motility and Cytokinesis. *Dev. Cell.* 35:725–736. https://doi.org/10.1016/j.devcel.2015.11.023

McDonald, N.A., Y. Takizawa, A. Feoktistova, P. Xu, M.D. Ohi, C.W. Vander Kooi, and K.L. Gould. 2016. The Tubulation Activity of a Fission Yeast F-BAR Protein Is Dispensable for Its Function in Cytokinesis. *Cell Reports.* 14:534–546. https://doi.org/10.1016/j.celrep.2015.12.062

Meinecke, M., E. Boucrot, G. Camdere, W.C. Hon, R. Mittal, and H.T. McMahon. 2013. Cooperative recruitment of dynamin and BIN/amphiphysin/Rvs (BAR) domain-containing proteins leads to GTP-dependent membrane scission. *J. Biol. Chem.* 288:6651–6661. https://doi.org/10.1074/jbc.M112.444869

Meitinger, F., M.E. Boehm, A. Hofmann, B. Hub, H. Zentgraf, W.D. Lehmann, and G. Pereira. 2011. Phosphorylation-dependent regulation of the F-BAR protein Hof1 during cytokinesis. *Genes Dev.* 25:875–888. https://doi.org/10.1101/gad.622411

Miele, A.E., P.J. Watson, P.R. Evans, L.M. Traub, and D.J. Owen. 2004. Two distinct interaction motifs in amphiphysin bind two independent sites

on the clathrin terminal domain beta-propeller. *Nat. Struct. Mol. Biol.* 11:242–248. https://doi.org/10.1038/nsmb736

Mierzwa, B., and D.W. Gerlich. 2014. Cytokinetic abscission: molecular mechanisms and temporal control. *Dev. Cell.* 31:525–538. https://doi.org/10.1016/j.devcel.2014.11.006

Mim, C., and V.M. Unger. 2012. Membrane curvature and its generation by BAR proteins. *Trends Biochem. Sci.* 37:526–533. https://doi.org/10.1016/j.tibs.2012.09.001

Mim, C., H. Cui, J.A. Gawronski-Salerno, A. Frost, E. Lyman, G.A. Voth, and V.M. Unger. 2012. Structural basis of membrane bending by the N-BAR protein endophilin. *Cell.* 149:137–145. https://doi.org/10.1016/j.cell.2012.01.048

Momin, N., S. Lee, A.K. Gadok, D.J. Busch, G.D. Bachand, C.C. Hayden, J.C. Stachowiak, and D.Y. Sasaki. 2015. Designing lipids for selective partitioning into liquid ordered membrane domains. *Soft Matter.* 11:3241–3250. https://doi.org/10.1039/C4SM02856B

Neumann, S., and S.L. Schmid. 2013. Dual role of BAR domain-containing proteins in regulating vesicle release catalyzed by the GTPase, dynamin-2. *J. Biol. Chem.* 288:25119–25128. https://doi.org/10.1074/jbc.M113.490474

Neumann, S., T.J. Pucadyil, and S.L. Schmid. 2013. Analyzing membrane remodeling and fission using supported bilayers with excess membrane reservoir. *Nat. Protoc.* 8:213–222. https://doi.org/10.1038/nprot.2012.152

Owen, D.J., P. Wigge, Y. Vallis, J.D. Moore, P.R. Evans, and H.T. McMahon. 1998. Crystal structure of the amphiphysin-2 SH3 domain and its role in the prevention of dynamin ring formation. *EMBO J.* 17:5273–5285. https://doi.org/10.1093/emboj/17.18.5273

Owen, D.J., B.M. Collins, and P.R. Evans. 2004. Adaptors for clathrin coats: structure and function. *Annu. Rev. Cell Dev. Biol.* 20:153–191. https://doi.org/10.1146/annurev.cellbio.20.010403.104543

Peter, B.J., H.M. Kent, I.G. Mills, Y. Vallis, P.J. Butler, P.R. Evans, and H.T. McMahon. 2004. BAR domains as sensors of membrane curvature: the amphiphysin BAR structure. *Science.* 303:495–499. https://doi.org/10.1126/science.1092586

Pietrosemoli, N., R. Pancsa, and P. Tompa. 2013. Structural disorder provides increased adaptability for vesicle trafficking pathways. *PLOS Comput. Biol.* 9:e1003144. https://doi.org/10.1371/journal.pcbi.1003144

Pocivavsek, L., K. Gavrilov, K.D. Cao, E.Y. Chi, D. Li, B. Lin, M. Meron, J. Majewski, and K.Y. Lee. 2011. Glycerol-induced membrane stiffening: the role of viscous fluid adlayers. *Biophys. J.* 101:118–127. https://doi.org/10.1016/j.bpj.2011.05.036

Poudel, K.R., Y. Dong, H. Yu, A. Su, T. Ho, Y. Liu, K. Schulten, and J. Bai. 2016. A time course of orchestrated endophilin action in sensing, bending, and stabilizing curved membranes. *Mol. Biol. Cell.* 27:2119–2132. https://doi.org/10.1091/mbc.e16-04-0264

Pucadyil, T.J., and S.L. Schmid. 2008. Real-time visualization of dynamin-catalyzed membrane fission and vesicle release. *Cell.* 135:1263–1275. https://doi.org/10.1016/j.cell.2008.11.020

Ramachandran, R., and S.L. Schmid. 2018. The dynamin superfamily. *Curr. Biol.* 28:R411–R416. https://doi.org/10.1016/j.cub.2017.12.013

Reider, A., S.L. Barker, S.K. Mishra, Y.J. Im, L. Maldonado-Báez, J.H. Hurley, L.M. Traub, and B. Wendland. 2009. Syp1 is a conserved endocytic adaptor that contains domains involved in cargo selection and membrane tubulation. *EMBO J.* 28:3103–3116. https://doi.org/10.1038/emboj.2009.248

Ren, G., P. Vajjhala, J.S. Lee, B. Winsor, and A.L. Munn. 2006. The BAR domain proteins: molding membranes in fission, fusion, and phagy. *Microbiol. Mol. Biol. Rev.* 70:37–120. https://doi.org/10.1128/MMBR.70.1.37-120.2006

Renard, H.F., M. Simunovic, J. Lemière, E. Boucrot, M.D. Garcia-Castillo, S. Arumugam, V. Chambon, C. Lamaze, C. Wunder, A.K. Kenworthy, et al. 2015. Endophilin-A2 functions in membrane scission in clathrin-independent endocytosis. *Nature.* 517:493–496. https://doi.org/10.1038/nature14064

Roberts-Galbraith, R.H., and K.L. Gould. 2010. Setting the F-BAR: functions and regulation of the F-BAR protein family. *Cell Cycle.* 9:4091–4097. https://doi.org/10.4161/cc.9.20.13587

Roberts-Galbraith, R.H., M.D. Ohi, B.A. Ballif, J.S. Chen, I. McLeod, W.H. McDonald, S.P. Gygi, J.R. Yates III, and K.L. Gould. 2010. Dephosphorylation of F-BAR protein Cdc15 modulates its conformation and stimulates its scaffolding activity at the cell division site. *Mol. Cell.* 39:86–99. https://doi.org/10.1016/j.molcel.2010.06.012

Ruiz-Taylor, L.A., T.L. Martin, F.G. Zaugg, K. Witte, P. Indermuhle, S. Nock, and P. Wagner. 2001. Monolayers of derivatized poly(L-lysine)-grafted poly(ethylene glycol) on metal oxides as a class of biomolecular interfaces. *Proc. Natl. Acad. Sci. USA.* 98:852–857. https://doi.org/10.1073/pnas.98.3.852

Saarikangas, J., H. Zhao, A. Pykäläinen, P. Laurinmäki, P.K. Mattila, P.K. Kinnunen, S.J. Butcher, and P. Lappalainen. 2009. Molecular mechanisms of membrane deformation by I-BAR domain proteins. *Curr. Biol.* 19:95–107. https://doi.org/10.1016/j.cub.2008.12.029

Salzer, U., J. Kostan, and K. Djinović-Carugo. 2017. Deciphering the BAR code of membrane modulators. *Cell. Mol. Life Sci.* 74:2413–2438. https://doi.org/10.1007/s00018-017-2478-0

Sherman, E., and G. Haran. 2006. Coil-globule transition in the denatured state of a small protein. *Proc. Natl. Acad. Sci. USA.* 103:11539–11543. https://doi.org/10.1073/pnas.0601395103

Simunovic, M., G.A. Voth, A. Callan-Jones, and P. Bassereau. 2015. When Physics Takes Over: BAR Proteins and Membrane Curvature. *Trends Cell Biol.* 25:780–792. https://doi.org/10.1016/j.tcb.2015.09.005

Simunovic, M., E. Evergren, I. Golushko, C. Prévost, H.F. Renard, L. Johannes, H.T. McMahon, V. Lorman, G.A. Voth, and P. Bassereau. 2016. How curvature-generating proteins build scaffolds on membrane nanotubes. *Proc. Natl. Acad. Sci. USA.* 113:11226–11231. https://doi.org/10.1073/pnas.1606943113

Simunovic, M., J.B. Manneville, H.F. Renard, E. Evergren, K. Raghunathan, D. Bhatia, A.K. Kenworthy, G.A. Voth, J. Prost, H.T. McMahon, et al. 2017. Friction Mediates Scission of Tubular Membranes Scaffolded by BAR Proteins. *Cell.* 170:172–184.e11. https://doi.org/10.1016/j.cell.2017.05.047

Smaczynska-de Rooij, I.I., E.G. Allwood, S. Aghamohammadzadeh, E.H. Hettema, M.W. Goldberg, and K.R. Ayscough. 2010. A role for the dynamin-like protein Vps1 during endocytosis in yeast. *J. Cell Sci.* 123:3496–3506. https://doi.org/10.1242/jcs.070508

Snead, W.T., C.C. Hayden, A.K. Gadok, C. Zhao, E.M. Lafer, P. Rangamani, and J.C. Stachowiak. 2017. Membrane fission by protein crowding. *Proc. Natl. Acad. Sci. USA.* 114:E3258–E3267. https://doi.org/10.1073/pnas.1616199114

Sorre, B., A. Callan-Jones, J. Manzi, B. Goud, J. Prost, P. Bassereau, and A. Roux. 2012. Nature of curvature coupling of amphiphysin with membranes depends on its bound density. *Proc. Natl. Acad. Sci. USA.* 109:173–178. https://doi.org/10.1073/pnas.1103594108

Srinivasan, N., M. Bhagawati, B. Ananthanarayanan, and S. Kumar. 2014. Stimuli-sensitive intrinsically disordered protein brushes. *Nat. Commun.* 5:5145. https://doi.org/10.1038/ncomms6145

Stachowiak, J.C., C.C. Hayden, and D.Y. Sasaki. 2010. Steric confinement of proteins on lipid membranes can drive curvature and tubulation. *Proc. Natl. Acad. Sci. USA.* 107:7781–7786. https://doi.org/10.1073/pnas.0913306107

Stachowiak, J.C., E.M. Schmid, C.J. Ryan, H.S. Ann, D.Y. Sasaki, M.B. Sherman, P.L. Geissler, D.A. Fletcher, and C.C. Hayden. 2012. Membrane bending by protein-protein crowding. *Nat. Cell Biol.* 14:944–949. https://doi.org/10.1038/ncb2561

Stamou, D., C. Duschl, E. Delamarche, and H. Vogel. 2003. Self-assembled microarrays of attoliter molecular vessels. *Angew. Chem. Int. Ed. Engl.* 42:5580–5583. https://doi.org/10.1002/anie.200351866

Takei, K., V.I. Slepnev, V. Haucke, and P. De Camilli. 1999. Functional partnership between amphiphysin and dynamin in clathrin-mediated endocytosis. *Nat. Cell Biol.* 1:33–39. https://doi.org/10.1038/9004

Taylor, M.J., D. Perrais, and C.J. Merrifield. 2011. A high precision survey of the molecular dynamics of mammalian clathrin-mediated endocytosis. *PLoS Biol.* 9:e1000604. https://doi.org/10.1371/journal.pbio.1000604

Umasankar, P.K., L. Ma, J.R. Thieman, A. Jha, B. Doray, S.C. Watkins, and L.M. Traub. 2014. A clathrin coat assembly role for the muniscin protein central linker revealed by TALEN-mediated gene editing. *eLife.* 3:e04137. https://doi.org/10.7554/eLife.04137

Vennema, H., G.J. Godeke, J.W. Rossen, W.F. Voorhout, M.C. Horzinek, D.J. Opstelten, and P.J. Rottier. 1996. Nucleocapsid-independent assembly of coronavirus-like particles by co-expression of viral envelope protein genes. *EMBO J.* 15:2020–2028. https://doi.org/10.1002/j.1460-2075.1996.tb00553.x

Wang, L., A. Johnson, M. Hanna, and A. Audhya. 2016. Eps15 membrane-binding and -bending activity acts redundantly with Fcho1 during clathrin-mediated endocytosis. *Mol. Biol. Cell.* 27:2675–2687. https://doi.org/10.1091/mbc.e16-03-0151

Wigge, P., K. Köhler, Y. Vallis, C.A. Doyle, D. Owen, S.P. Hunt, and H.T. McMahon. 1997. Amphiphysin heterodimers: potential role in clathrin-mediated endocytosis. *Mol. Biol. Cell.* 8:2003–2015. https://doi.org/10.1091/mbc.8.10.2003

Wu, T., Z. Shi, and T. Baumgart. 2014. Mutations in BIN1 associated with centronuclear myopathy disrupt membrane remodeling by affecting protein density and oligomerization. *PLoS One.* 9:e93060. https://doi.org/10.1371/journal.pone.0093060

Wuertenberger, S., and Y. Groemping. 2015. A single PXXP motif in the C-terminal region of srGAP3 mediates binding to multiple SH3 domains. *FEBS Lett.* 589:1156–1163. https://doi.org/10.1016/j.febslet.2015.03.014

Zhang, H., and S. Han. 1996. Viscosity and density of water plus sodium chloride plus potassium chloride solutions at 298.15 K. *J. Chem. Eng. Data.* 41:516–520. https://doi.org/10.1021/je9501402

Zimmerberg, J., and M.M. Kozlov. 2006. How proteins produce cellular membrane curvature. *Nat. Rev. Mol. Cell Biol.* 7:9–19. https://doi.org/10.1038/nrm1784